bioRxiv preprint doi: https://doi.org/10.1101/022962; this version posted July 21, 2015. The copyright holder for this preprint (which was not certified by peer review) is the author/funder. All rights reserved. No reuse allowed without permission.

Nanoscale architecture of the axon initial segment reveals an organized and robust scaffold

Christophe Leterrier[1]*, Jean Potier[1], Ghislaine Caillol[1], Fanny Rueda Boroni[1], Bénédicte Dargent[1]

[1] Aix Marseille Université, CNRS, CRN2M UMR7286, 13344 cedex 15, Marseille, France

* corresponding author: christophe.leterrier@univ-amu.fr

The Axon Initial Segment [AIS], located within the first 30 µm of the axon, has two essential roles: generating the action potential, and maintaining axonal identity. AIS assembly depends on an ankyrin G / ßIV-spectrin scaffold, but its macromolecular arrangement is unknown, precluding the mechanistic understanding of its functions. We quantitatively determined the AIS nanoscale architecture using STochastic Optical Reconstruction Microscopy [STORM]. First, we directly demonstrated the existence of an AIS 190-nm periodic submembrane lattice composed of alternated actin rings and ßIV-spectrin dimers. Next, we used antibodies against different domains of ankyrin G to map its 3D nanoscale positioning: multicolor STORM demonstrated that the two large isoforms of ankyrin G are radially oriented across the AIS, with a 30-nm radial extent. The robustness of the AIS nano-architecture features against cytoskeletal or pharmacological perturbations suggest their structural role in the overall stability of the compartment. This organized and robust nanoscale architecture likely underpins the AIS functions in physiological and pathological contexts.

axon initial segment | cytoskeleton | ankyrin G | super-resolution microscopy

Introduction

The directional flow of information in the brain is ensured by the cellular asymmetry of the neuron: the neuronal cell body receives synaptic inputs, and the axon propagates the action potential to downstream neurons. Once polarity is established, the neuronal asymmetry must be maintained for years or even decades. This is done through a combination of passive (barriers) and active (directed traffic) processes, but the underpinning mechanisms remain largely unknown (Kapitein and Hoogenraad, 2011). Located along the first 20 to 40 µm of the axon, the Axon Initial Segment [AIS] materializes the separation between the somatodendritic and axonal compartments. This location allows for the two main cellular functions of the AIS: the initiation of action potentials, and the maintenance of axonal identity (Leterrier and Dargent, 2014). Importantly, perturbed AIS morphology and functions have been implicated in several psychiatric and neurodegenerative disorders (Hsu et al., 2014).

The AIS ensures the proper generation and modulation of action potentials by concentrating voltage-gated ion channels at its surface: sodium Nav, potassium KCNQ. Together with specific cell adhesion molecules, these channels are anchored at the AIS by their interaction with a specialized scaffold protein, ankyrin G [ankG], which also binds to a submembrane complex of ßIV-spectrin and actin (for reviews see Bennett and Lorenzo, 2013; Normand and Rasband, 2015; Grubb and Burrone, 2010b; Leterrier and Dargent, 2014). Furthermore, ankG links the AIS scaffold to microtubule fascicles, via an interaction with end-binding proteins EB1/3 (Leterrier et al., 2011). AnkG is the AIS master organizer: it first localizes along the proximal axon (Galiano et al., 2012), then recruits and concentrates its partners. Consequently, depletion of ankG results in the absence or disassembly of the whole AIS complex (Jenkins and Bennett, 2001; Hedstrom et al., 2007; 2008). These studies demonstrated the role of the AIS for the maintenance of axonal identity: in ankG-depleted neurons that lack an AIS, somatodendritic proteins progressively invade the proximal axon, resulting in the disappearance of microtubules fascicles, and the formation of ectopic post-synapses (Hedstrom et al., 2008; Sobotzik et al., 2009).

Two proposed cellular processes contribute to this maintenance of axonal identity: a surface diffusion barrier that restricts the mobility of membrane proteins and lipids (Winckler et al., 1999; Nakada et al., 2003), and a traffic filter that could control the intracellular diffusion and transport (Song et al., 2009). The underlying mechanisms are still mysterious, in particular the nature of the intracellular filter (Watanabe et al., 2012; Petersen et al., 2014). Our understanding of these processes depends on a better knowledge of the AIS architecture down to the molecular level. Super-resolution microscopy now allows to observe macromolecular complexes in situ with a few tens of nanometers resolution (Maglione and Sigrist, 2013), and has recently led to a few key advances in our understanding of the AIS organization. Using STochastic Optical Reconstruction Microscopy [STORM], the Zhuang lab showed that the AIS and axonal actin is organized as submembrane rings periodically spaced every 190 nm (Xu et al., 2013), a result confirmed recently in living cells using STimulated Emission Depletion [STED] microscopy (D'Este et al., 2015). In the AIS, a periodic arrangement of actin, ßIV-spectrin and ankG could also be detected (Zhong et al., 2014). Besides, electron microscopy was used to resolve individual AIS proteins such as ankG and ßIV-spectrin in detergent-extracted cells, showing that these proteins adopt 50 to 150 nm-long filament or rod conformations (Jones et al., 2014).

We set about quantitatively resolving the three-dimensional architecture of the AIS at the nanoscale level, in particular the arrangement of the two large isoforms of the master scaffold protein ankG (Jenkins et al., 2015). Multicolor 2D- and 3D-STORM of endogenous epitopes, coupled to extensive quantification procedures, allowed us to uncover the intricate ordering of the AIS scaffold: we directly demonstrate that a periodic lattice of ßIV-spectrin dimers connects actin rings along the AIS. AnkG links this lattice with intracellular components by adopting a radial orientation between the plasma membrane and the axoplasm. Finally, our observations reveal an unexpected robustness of the AIS scaffold: its ordered arrangement is resistant to pharmacological perturbations of the actin or microtubule cytoskeleton. Treatments that significantly disassemble the whole AIS, such as elevated intracellular calcium, only partially alter its organization, suggesting the intrinsic structural role of this nano-architecture.

Results

Actin and longitudinal ßIV-spectrin dimers form the AIS periodic submembrane lattice

To characterize the AIS nano-architecture, we first focused on the organization of the submembrane actin/ßIV-spectrin complex. At the diffraction-limited level, actin was present but not concentrated in the AIS of mature neurons (15 to 21 days in vitro [div]), in contrast to ßIV-spectrin and voltage-gated sodium (Nav) channels (Fig. 1A). STORM images revealed the periodic arrangement of AIS actin as regular bands (Fig. 1B-C), as described recently (Xu et al., 2013; D'Este et al., 2015; Zhong et al., 2014). Line profiles obtained on 2D-STORM images exhibited intensity peaks with a regular spacing of ~190 nm (Fig. 1D). We quantified the labeling periodicity by fitting sinusoids on 1 µm-long intensity profiles,

bioRxiv preprint doi: https://doi.org/10.1101/022962; this version posted July 21, 2015. The copyright holder for this preprint (which was not certified by peer review) is the author/funder. All rights reserved. No reuse allowed without permission.

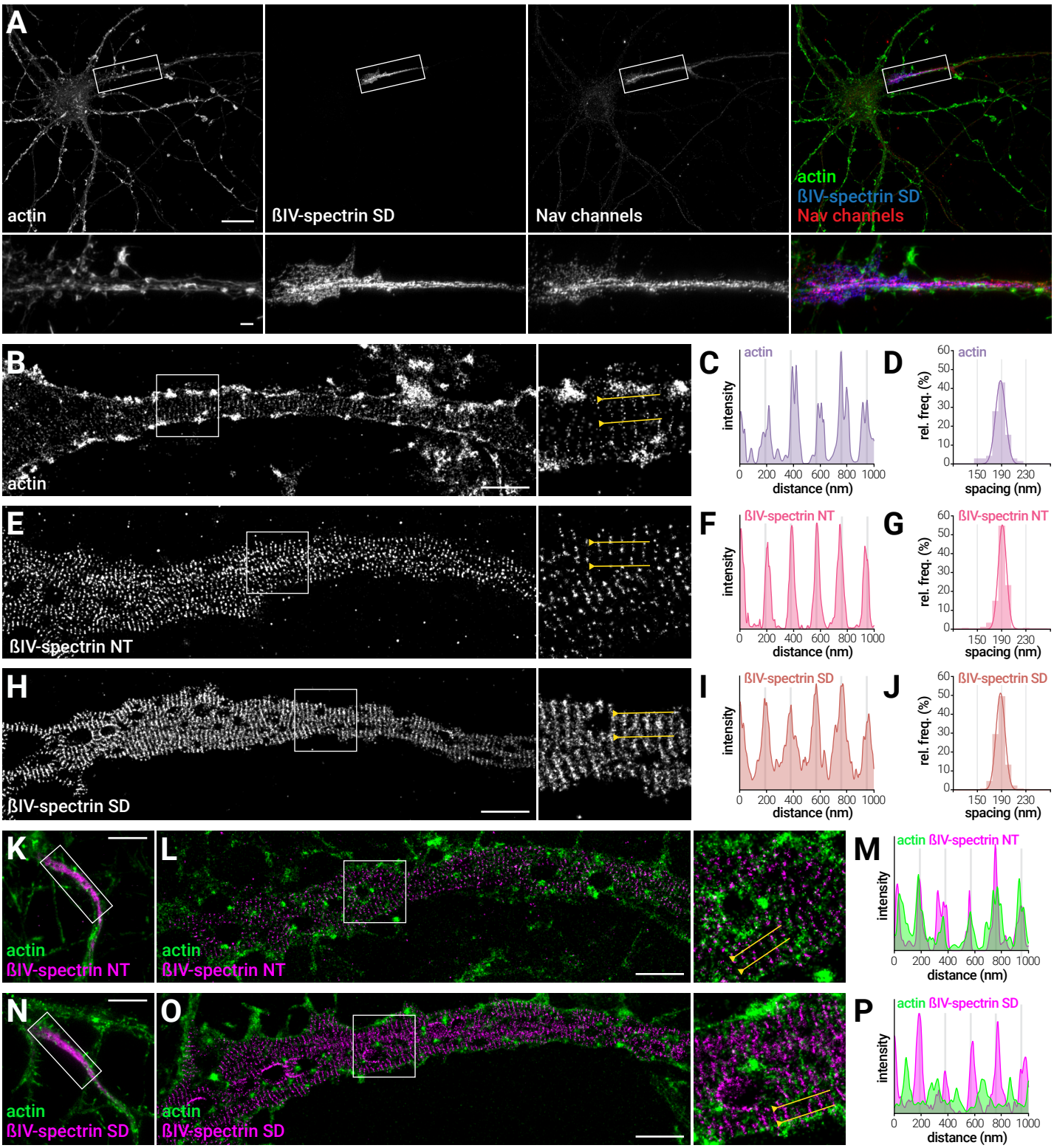

Figure 1. Actin and longitudinal ßIV-spectrin dimers form the AIS periodic submembrane lattice

(A) Epifluorescence image of a neuron labeled for actin (green), ßIV-spectrin SD (blue) and Nav channels (red). Scale bar 20 µm (image), 2 µm (zoom). (B-D) STORM image of an AIS labeled for actin (B). For (B), (E), (H), (L) and (O), scale bar is 2 µm. Intensity profile along the yellow line (C, gray vertical lines are 190 nm apart). Histogram of the spacing values (D, n=72 profiles, N=3). (E-G) STORM image of an AIS labeled for ßIV-spectrin NTer (E), corresponding intensity profile (F), and histogram of the spacing values (G, n=183, N=3). (H-J) STORM image of an AIS labeled for ßIV-spectrin SD (H), corresponding intensity profile (I), and histogram of the spacing values (J, n=334, N=11). (K-M) Epifluorescence image of a neuron labeled for actin (green) and ßIV-spectrin NT (magenta) (K). For (K) and (N), scale bar is 10 µm. 2-color STORM image of its AIS (L), and corresponding intensity profile (M). (N-P) Epifluorescence image of neuron labeled for actin (green) and ßIV-spectrin SD (magenta)(N), 2-color STORM image of its AIS (O), and corresponding intensity profile (P).

bioRxiv preprint doi: https://doi.org/10.1101/022962; this version posted July 21, 2015. The copyright holder for this preprint (which was not certified by peer review) is the author/funder. All rights reserved. No reuse allowed without permission.

and fitting of the resulting spacing values histogram with a Gaussian curve (Fig. S1). The mean spacing and its spread were measured at 188 ± 8 nm for actin labeling along the AIS (see Table S1). We next assessed the distribution of ßIV-spectrin using an antibody against its aminoterminus [NT], which contains the binding site with actin (Bennett and Lorenzo, 2013). ßIV-spectrin NT exhibited a strikingly periodic labeling pattern (Fig. 1E-F), and we measured the spacing distribution at 191 ± 7 nm (Fig. 1G), in close agreement with the value reported previously (Xu et al., 2013). We determined the distribution of the other side of ßIV-spectrin, using an antibody against its specific domain [SD], close to the carboxyterminus (Bennett and Lorenzo, 2013). Similar to ßIV-spectrin NT, the ßIV-spectrin SD distribution was highly periodic, with a 188 ± 8 nm average spacing (Fig. 1H-I). Spacing spread was only slightly lower for ßIV-spectrin NT (7 nm, versus 8 nm for SD) and goodness of fit values were similar (mean R squared of sinusoid fits, 0.55 and 0.57 for NT and SD respectively, see Table S1), consistent with a model of regular assemblies of horizontal ßIV-spectrin dimers connecting actin rings (see cartoon in Fig. S2F).

To further clarify the organization of actin and ßIV-spectrin, we next used two-color STORM to determine the relative localization of AIS epitopes. First, we could detect a periodic distribution of Nav channel clusters along the AIS (spacing 190 ± 16 nm, Fig. S2A-C). Two-color STORM revealed the colocalization of these Nav clusters with ßIV-spectrin SD (Fig. S2D-E), in contrast to their complementary localization relative to the ßIV-spectrin NT pattern (as shown in Xu et al., 2013), indirectly confirming the actin rings/spectrin dimers model. Direct demonstration was obtained by using Atto 488-coupled phalloidin to simultaneously image actin and ßIV-spectrin epitopes (Fig. 1K-P). Although similar at the

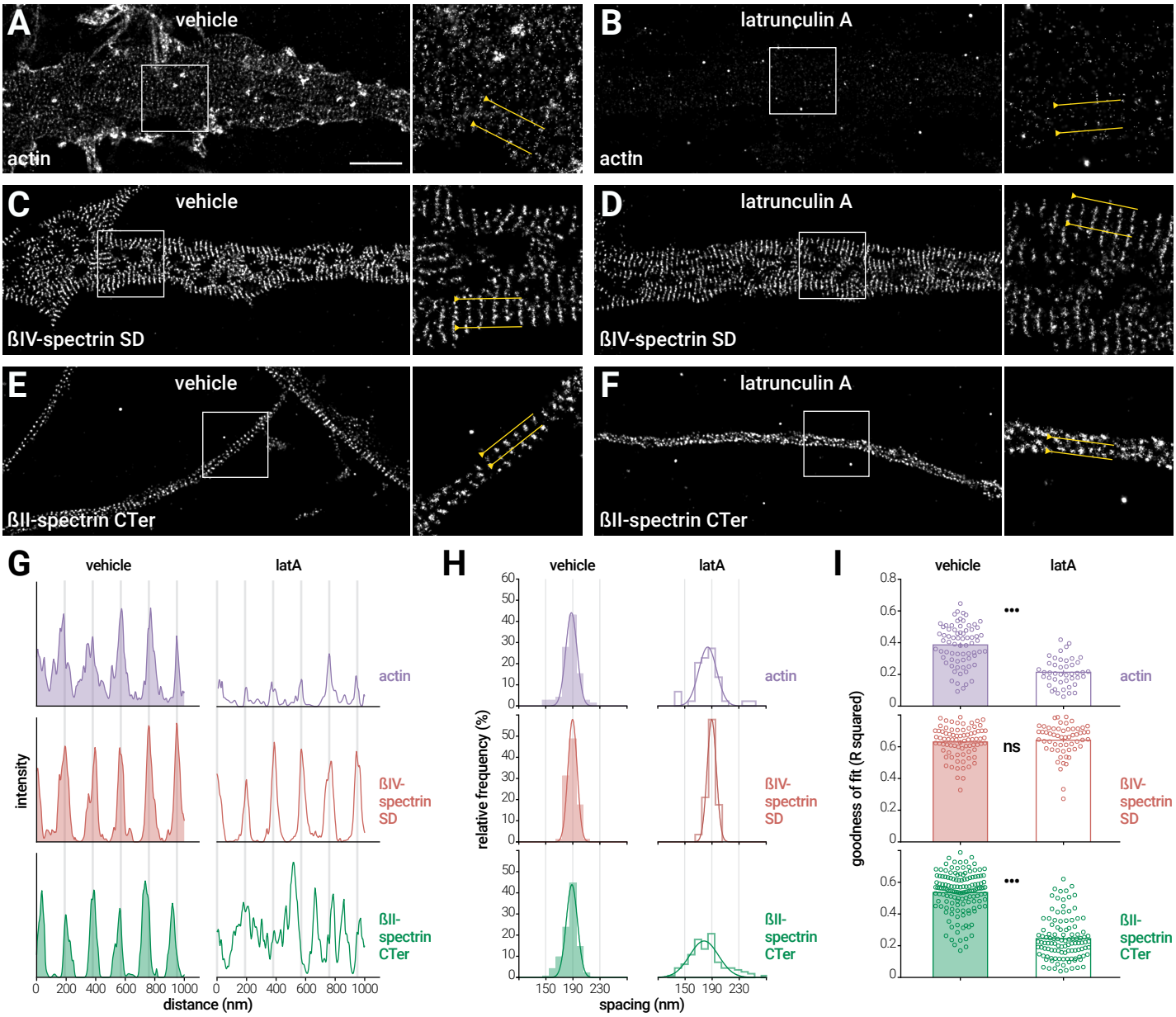

Figure 2. The AIS submembrane lattice is resistant to actin perturbation
(A-F) STORM image of the AIS from neurons treated with vehicle (DMSO 0.1%, 1h) (A) or latA (5µM, 1h) (B), fixed and labeled for actin. For (A-F), scale bar is 2 µm. Distal axons of neurons treated with vehicle (C) or latA (D), fixed and labeled for ßII-spectrin CTer. AIS of neurons treated with vehicle (E), or latA (F), fixed and labeled for ßIV-spectrin SD. (G) Intensity profiles along the yellow lines in (A-F) for the actin (purple), ßII-spectrin CTer (green) and ßIV-spectrin SD (red) labeling, after treatment with vehicle (left) or latA (right). (H-I) Histograms of the spacing values for each labeling, after treatment with vehicle or latA (H, n=44-143 profiles, N=3-4). Goodness of sinusoid fit (R squared) for each labeling, after treatment with vehicle or latA (I, n=44-143, N=3-4).

bioRxiv preprint doi: https://doi.org/10.1101/022962; this version posted July 21, 2015. The copyright holder for this preprint (which was not certified by peer review) is the author/funder. All rights reserved. No reuse allowed without permission.

diffraction-limited level (Fig. 1K & 1N), on STORM images the periodic ßIV-spectrin NT bands colocalized with actin bands (Fig. 1L-M), whereas the ßIV-spectrin SD bands were complementary to actin bands (Fig. 1O-P). This differential position of ßIV-spectrin ends relative to actin rings directly demonstrates the longitudinal, periodic organization of ßIV-spectrin dimers between actin rings along the AIS (Fig. S2F).

The AIS submembrane lattice is resistant to actin perturbation

The AIS scaffold is remarkably stable over time (Hedstrom et al., 2008). We wondered if the ßIV-spectrin periodic lattice would nonetheless depend on integrity of the actin structure. To test this hypothesis, we assessed the ßIV-spectrin nanoscale distribution after actin depolymerization by latrunculin A [latA]. Treatment with 5 µM latA for one hour almost completely disassembled actin filaments in all compartments, with a disappearance of phalloidin labeling on diffraction-limited images (Fig. S3).

STORM images revealed the disorganization of actin in the AIS, although a faint remnant of actin periodicity could still be detected, suggesting a selective resistance to depolymerization (Fig. 2A-B & 2G). Strikingly, the periodic pattern of the ßIV-spectrin SD was unaffected by latA treatment (Fig. 2C-D & 2G). In the control condition, actin and ßIV-spectrin in the AIS exhibited an identical spacing of 188 ± 8 nm (Fig. 2H). After latA treatment, the spread of the spacing remained stable for ßIV-spectrin (190 ± 7 nm). Actin showed a significant drop in the goodness of sinusoid fit after latA treatment, indicating a loss of periodicity (from 0.39 ± 0.02 to 0.21 ± 0.01, mean ± SEM), but the goodness of fit for ßIV-spectrin remained high after actin depolymerization (0.63 ± 0.01 for vehicle, 0.64 ± 0.01 for latA, Fig. 2I). Thus, ßIV-spectrin periodic organization in the AIS is resistant to actin perturbation.

To determine if this resistance is specific to the AIS, we compared it to the effect of actin disruption on the distal actin/spectrin complex, which forms a similar periodic structure, with ßII-spectrin instead of the AIS-specific ßIV-spectrin (Xu et al., 2013). Using an antibody against the

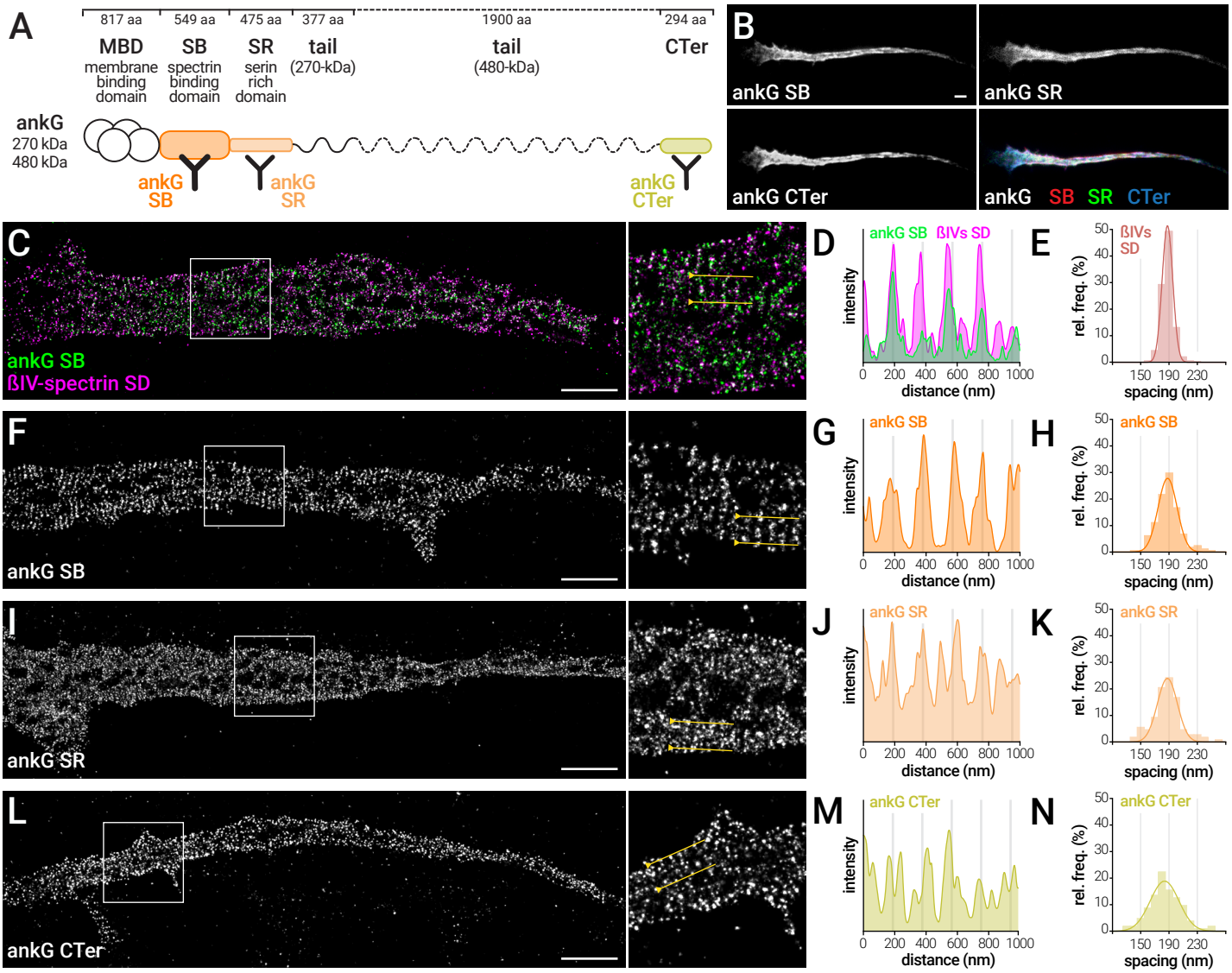

Figure 3. AnkG associates with the periodic spectrin lattice, but becomes disordered away from the spectrin binding site
(A) Cartoon of the ankG isoforms found at the AIS. Target domains of the three anti-ankG antibodies used are indicated. (B) Epifluorescence image showing the AIS of neuron labeled for ankG SB (red), ankG SR (green), and ankG CTer (blue). Scale bar, 5 µm. (C-D) STORM image of an AIS labeled for ankG SB (green) and ßIV-spectrin SD (magenta) (C). For (C), (F), (I) and (L), scale bar is 2 µm. Intensity profiles for each channel along the yellow line (D). (E) Histogram of the spacing values for the ßIV-spectrin SD labeling (same data as in Figure 1J). (F-H) STORM image of an AIS labeled for ankG SB (F), corresponding intensity profile (G), and histogram of the spacing values (H, n=161 profiles, N =6). (I-K) STORM image of an AIS labeled for ankG SR (I), corresponding intensity profile (J), and histogram of the spacing values (K, n=107, N =3). (L-N) STORM image of an AIS labeled for ankG CTer (L), corresponding intensity profile (M), and histogram of the spacing values (N, n=102, N =4).

bioRxiv preprint doi: https://doi.org/10.1101/022962; this version posted July 21, 2015. The copyright holder for this preprint (which was not certified by peer review) is the author/funder. All rights reserved. No reuse allowed without permission.

ßII-spectrin carboxyterminus (CTer), we indeed found a highly periodic distribution along distal axons, with a regular spacing of 188 ± 8 nm (Fig. 2E & 2G). ßII-spectrin was still clustered after LatA treatment, but the regular spacing was disorganized, with a rising spacing spread (190 ± 22 nm, Fig. 2H), and a drop of the sinusoid fit R squared from 0.54 ± 0.01 to 0.25 ± 0.01 (Fig. 2I), confirming previous results (Xu et al., 2013; Zhong et al., 2014). In conclusion, the ßIV-spectrin periodic lattice in the AIS is specifically resistant to actin perturbation, compared to the ßII-spectrin complex found in the distal axon.

AnkG associates with the periodic spectrin lattice, but becomes disordered away from the spectrin binding site

What makes the ßIV-spectrin/actin lattice in the AIS more resistant than the ßII-spectrin/actin complex along the distal axon? Interaction with ankG is a likely candidate, being the master organizer of the AIS, necessary for the recruitment and maintenance of ßIV-spectrin and other AIS components (Yang et al., 2007). The two ankG isoforms present at the AIS are large proteins of 270 and 480 kDa, that differ by a 1900 aminoacids insertion in the tail domain (Bennett and Lorenzo, 2013; Jenkins et al., 2015). To characterize the nanoscale organization of ankG in the AIS by STORM, we used antibodies directed against distinct domains that are present in both ankG isoforms (Fig. 3A). A polyclonal antibody directed against a peptide epitope in the serin-rich domain [SR] was previously described (Bréchet et al., 2008), and we mapped the target domains of two monoclonal antibodies (anti-ankG clone 106/65 and 106/36) to the spectrin-binding [SB] and carboxyterminal [CTer] domains, respectively (Fig. S4). These three antibodies labeled the AIS of hippocampal neurons in a similar fashion at the diffraction-limited level (Fig. 3B).

At the nanoscale level, we first localized the domain of ankG that interacts with ßIV-spectrin (the SB domain) together with ßIV-spectrin SD. Two-color STORM images show that the ankG SB clusters localized along ßIV-spectrin bands, resulting in correlated line profiles (Fig. 3C-D). We next compared the ankG SB domain distribution pattern to other ankG domains: the serin-rich domain (SR, localized adjacent to the SB domain) or the CTer domain (formed by the last 300 residues of the protein, Fig. 3A). On single color STORM images, the regular spacing of ankG SB clusters was clearly detected (Fig. 3F-G), as reflected by periodicity measurements (spacing 188 ± 13 nm, Fig. 3H and Table S1). Periodicity was similar for the adjacent SR domain (Fig. 3i-j), with a spacing of 188 ± 14 nm (Fig. 3K). The CTer domain exhibited some regularity in its organization, but a periodic pattern was more difficult to discern (Fig. 3L-M), and the spacing exhibited a significantly higher spread (184 ± 20 nm, Fig. 3N). Accordingly, the goodness of sinusoid fit (R squared) dropped from 0.34 ± 0.01 for the ankG SB domain, to 0.26 ± 0.01 for the SR and 0.22 ± 0.01 for the CTer domain (Table S1). This difference between the periodic distribution of the ankG SB domain and the aperiodic distribution of its CTer domain is consistent with a recent observation (Zhong et al., 2014). In conclusion, ankG exhibits a periodic arrangement of its aminoterminal side that interacts with ßIV-spectrin, but downstream domains, closer to its carboxyterminus, progressively loose this periodicity and become more disordered.

The ankG CTer domain penetrates in the axoplasm, resulting in a radial orientation of ankG

We hypothesized that the carboxyterminal part of ankG showed a disorganized distribution on 2D-STORM images, because it was located away from the periodic submembrane lattice: it could reach more intracellular partners deeper in the axoplasm. To test this, we resolved the transverse organization of the AIS using 3D-STORM (Huang et al., 2008). We first performed 3D-STORM of AIS labeled with ßIV-spectrin SD antibody, demonstrating the capacity to clearly visualize the AIS submembrane scaffold on transverse sections (Fig. 4A-B). To resolve the transverse organization of the AIS, we performed 2-color, 3D-STORM with different epitopes co-labeled with ßIV-spectrin SD as a reference (Fig. 4C-J). We first imaged two epitopes of proteins with expected distributions: membrane-bound Nav channels and intracellular microtubules. Nav channels colocalized with ßIV-spectrin on XY projections (Fig. 4C). On YZ transverse sections, they were found at the periphery of the ßIV-spectrin submembrane lattice (Fig. 4C), as confirmed by line profiles across transverse sections (Fig. 4D). α-tubulin labeling was not resolved as continuous microtubules on XY projections, due to the fixation protocol imposed by the ßIV-spectrin staining. Intracellular labeling for α-tubulin was nevertheless clear on transverse sections and line profiles, with the ßIV-spectrin lattice encasing the α-tubulin labeling (Fig. 4E-F).

Next, we assessed the transverse arrangement of ankG by imaging the two domains on opposite side of the protein (SB and CTer domains), together with ßIV-spectrin SD (Fig. 4G-J). Similar to Nav channels, the ankG SB domain colocalized with ßIV-spectrin bands on XY projections, and with the submembrane ßIV-spectrin lattice on transverse sections (Fig. 4G-H). The ankG CTer domain was found to be more intracellular than ßIV-spectrin: on transverse sections, the ankG CTer labeling was consistently found lining the intracellular side of the ßIV-spectrin lattice (Fig. 4I). On line profiles, this resulted in the ankG CTer intensity peaks being shifted toward the axoplasm compared to the ßIV-spectrin peaks (Fig. 4J). As AIS exhibit large variations in shape (length, transverse diameter, flatness), we devised a method to precisely quantify the radial arrangement of epitopes, independently of these variations. A Gaussian was fitted on line profiles across YZ sections, and the distance between the Gaussian maxima for the two channels was measured, resulting in a measure of the distance to the ßIV-spectrin SD reference for each epitope (Fig. S5). We determined the average distance between the ßIV-spectrin and the Nav channel III-IV loop to be 8 ± 1 nm (positive distance toward the axolemma, Fig. 4K and Table S2), whereas α-tubulin localization was broadly intracellular at -85 ± 4 nm (negative distance toward the axoplasm). The ankG SB domain was located just above ßIV-spectrin, with a mean distance of 6 ± 1 nm. The CTer domain of ankG was significantly more intracellular, with an average distance of -26 ± 1 nm to ßIV-spectrin (Fig. 4K). From these measurements, we determined that ankG had an average radial orientation in the AIS: its CTer domain was on average 32 ± 1 nm deeper than its SB domain. As an alternative visualization of this result, we aligned all line profiles relative to the maxima of the ßIV-spectrin reference channel, and generated mean intensity profiles for each labeling (Fig. 4L). This confirmed the ~32 nm inward extension between the ankG SB and CTer domains. In conclusion, we have showed that the AIS is not only organized longitudinally, but also transversally, with an average radial orientation of ankG between the plasma membrane and the axoplasm (see cartoon on Fig. 4M).

The 270- and 480-kDa isoforms of ankG have a similar radial extent in the AIS

The two large neuronal isoforms of ankG present in the AIS (480- and 270-kDa) differ by the insertion of a 1900 residues stretch in the unstructured tail region before the CTer domain. The anti-ankG antibodies used in our first experiments (SB, SR, CTer) recognize both isoforms (see Fig. 3A). 480- and 270-kDa ankG interact with membrane proteins on their aminoterminal side, so the apparently disordered distribution of the CTer domain could result from the carboxytermini of the two isoforms having distinct localizations. We used an antibody targeting the distal part of the 480-kDa specific tail, ~550 amino acids from the beginning of the CTer domain, to specifically assess the localization of the 480 kDa ankG carboxyterminal side. Anti-ankG 480tail (detecting the 480-kDa isoform) and ankG CTer (detecting both the 480- and 270-kDa isoforms) antibodies resulted in similar labeling at the diffraction-limited level, with a con-

bioRxiv preprint doi: https://doi.org/10.1101/022962; this version posted July 21, 2015. The copyright holder for this preprint (which was not certified by peer review) is the author/funder. All rights reserved. No reuse allowed without permission.

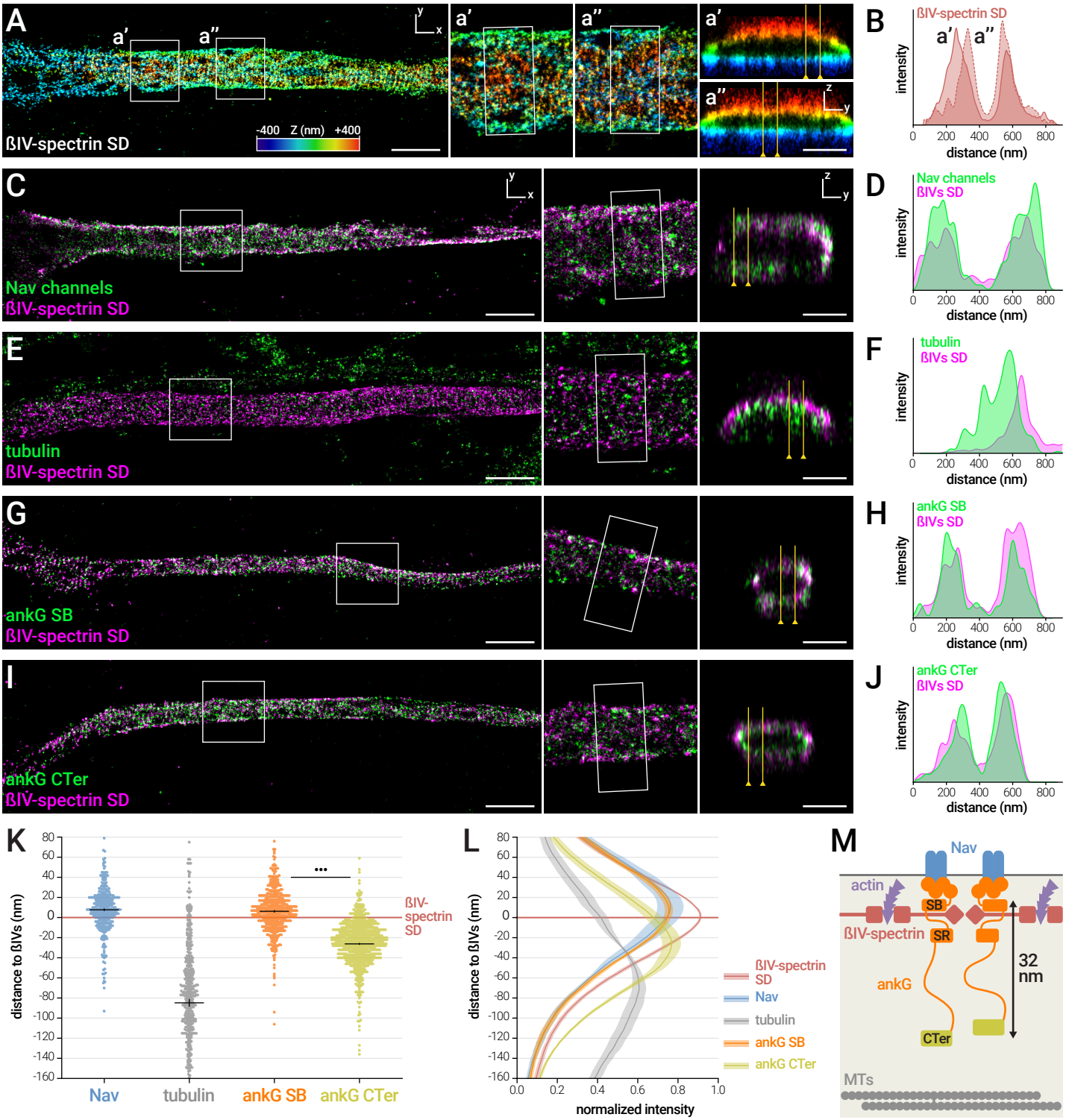

Figure 4. The ankG CTer domain penetrates in the axoplasm, resulting in a radial orientation of ankG

(A-B) 3D-STORM images of an AIS labeled for ßIV-spectrin SD (color-coded for depth) (A). Scale bar is 2 µm for XY images, 0.5 µm for YZ sections. Intensity profile along the yellow lines on the transverse sections (B). (C-D) 3D-STORM image of an AIS labeled for Nav channels (green) and ßIV-spectrin SD (magenta) (C), and corresponding intensity profiles (D). For (D), (F), (H), (J), profiles are taken along the yellow line on the corresponding transverse section shown. (E-F) 3D-STORM image of an AIS labeled for α-tubulin (green) and ßIV-spectrin SD (magenta) (E), and corresponding intensity profiles (F). (G-H) 3D-STORM image of an AIS labeled for ankG SB (green) and ßIV-spectrin SD (magenta) (G), and corresponding intensity profiles (H). (I-J) 3D-STORM image of an AIS labeled for ankG CTer (green) and ßIV-spectrin SD (magenta) (I), and corresponding intensity profiles (J). (K) Radial distance to ßIV-spectrin SD for the Nav, α-tubulin, ankG SB, and ankG CTer labeling. Red line is ßIV-spectrin SD reference at 0 nm (n=367-832 profiles, N=4-9). (L) Mean profiles for ßIV-spectrin SD (red), Nav channels (blue), α-tubulin (gray), ankG SB (orange) and ankG CTer (yellow, mean ± SEM of average profiles, N=4-5). (M) Structural model of the AIS radial organization.

bioRxiv preprint doi: https://doi.org/10.1101/022962; this version posted July 21, 2015. The copyright holder for this preprint (which was not certified by peer review) is the author/funder. All rights reserved. No reuse allowed without permission.

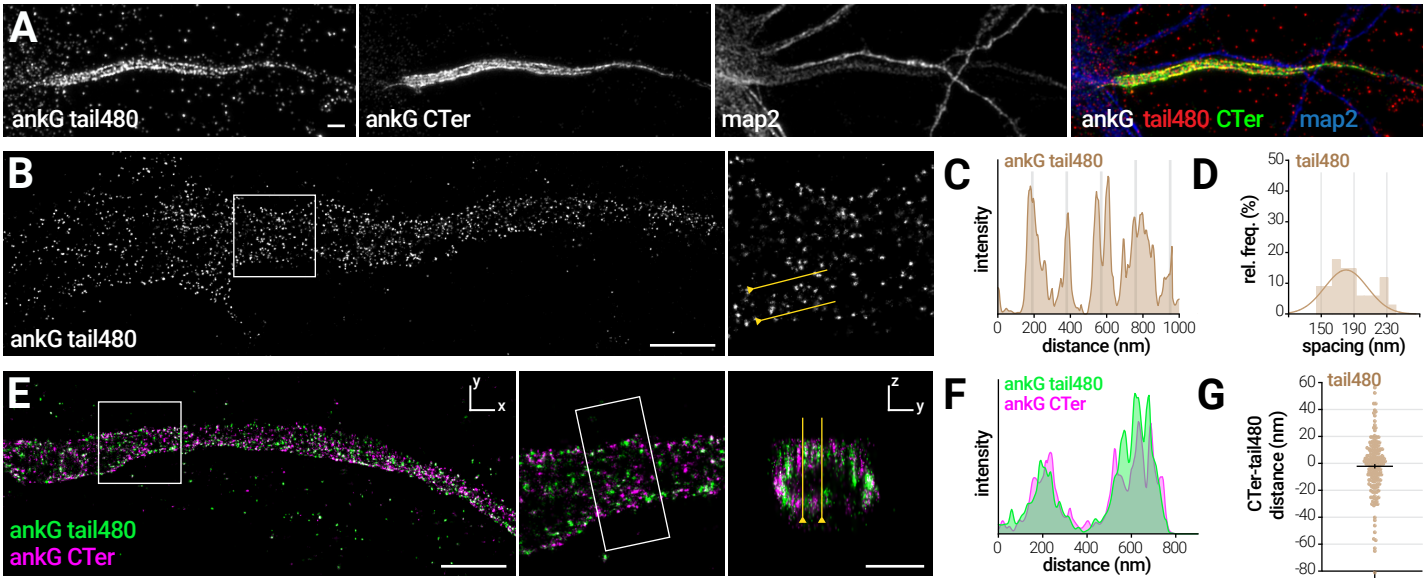

Figure 5. The 270- and 480-kDa isoforms of ankG have a similar radial extent in the AIS
(A) Deconvolved epifluorescence image of a neuron labeled for ankG tail480 (red), ankG CTer (green), and map2 (blue). Scale bar, 2 µm. (B-D) STORM image of an AIS labeled for ankG tail480 (B). Scale bar, 2 µm. Intensity profile along the yellow line (C), and histogram of the spacing values (D, n=34 profiles, N=2). (E-G) 3D-STORM image of an AIS labeled for ankG tail480 (green) and ankG CTer (magenta) (E). Scale bar is 2 µm for XY image, 0.5 µm for YZ section. Intensity profiles for each channel along the yellow line (F), and measurement of the radial distance between ankG tail480 and ankG CTer (G, n=168 profiles, N=2).

centration along the AIS of mature neurons (Fig. 5A). 2D-STORM images showed a punctate appearance of ankG 480tail along the AIS, with the rare detection of a periodic pattern (Fig. 5B-C). This distribution was similar to the ankG CTer labeling: quantification showed a high spread around the mean spacing at 182 ± 27 nm (Fig. 5D and Table S1). We then directly compared the radial localization of the ankG CTer domain with that of the ankG tail480 using 3D-STORM (Fig. 5E-F). Transverse sections showed that both labels were found at the same depth in the axon, with a measured distance between ankG CTer and the tail480 labeling close to zero at -2 ± 2 nm (Fig. 5G). The radial organization is thus common to both isoforms of ankG, and their similar radial extent could mean that the longer isoform adopts a more convoluted conformation of its unstructured tail.

Radial orientation of ankG is resistant to actin or microtubule perturbation

AnkG can be considered as a scaffold linker that binds both to actin via ßIV-spectrin, and to microtubules via EB1/3 proteins (Leterrier et al., 2011). Thus, we wondered if the ankG radial orientation was dependent on the actin or microtubule cytoskeleton integrity. First, we used latA to acutely perturb actin, and measured the radial distance between the ankG CTer domain and the ßIV-spectrin SD. LatA treatment (5 µM, 1h) did not modify ankG arrangement: the ankG CTer domain was still found deeper in the axon than ßIV-spectrin (Fig. 6A-B), with a distance of -26 ± 2 nm after treatment, compared to -24 ± 1 nm for vehicle (Fig. 6G and Table S2). Thus, ankG radial orientation does not depend on actin integrity.

Next, we used nocodazole at a high concentration (20 µM for 3h) to acutely disturb microtubules (Jaworski et al., 2009). At the diffraction-limited level, bundles of microtubules were disassembled in nocodazole treated neurons (Fig. S5A-B), with a few remaining filaments. STORM imaging after fixation with a protocol optimized for microtubule preservation showed that these remaining microtubules likely belonged to distal axons (Fig. S6C-D). Furthermore, the periodic ßIV-spectrin lattice was not perturbed by nocodazole treatment (Fig. S6E-H), with no change in spacing spread for the ßIV-spectrin SD labeling (187 ± 8 nm for both vehicle and nocodazole, Fig. S6E-J). This is in contrast with the partial disassembly of ßII-spectrin rings recently observed after nocodazole treatment by Zhong et al (Zhong et al., 2014), confirming the specific robustness of the AIS scaffold. Finally, we mapped the radial organization of ankG after nocodazole treatment. The localization of both the ankG SB and CTer domains was unaffected by nocodazole treatment: the ankG SB domain distance to ßIV-spectrin was 5 ± 2 nm for vehicle versus 5 ± 1 nm for nocodazole, whereas the ankG CTer domain distance was -24 ± 1 nm for vehicle, and -25 ± 1 nm for nocodazole (Fig. 6H-I). The longitudinal periodicity of the ßIV-spectrin lattice, as well as the radial ankG orientation, thus resist to actin filaments or microtubules perturbation.

The AIS nano-architecture is partially altered by inhibition of CK2 or elevated intracellular calcium

To further probe the robustness of the AIS scaffold organization at the nanoscale, we used treatments that could affect the AIS morphology without completely disassembling it. We have previously shown that inhibition of the protein kinase CK2 [CK2] by 2-dimethylamino-4,5,6,7-tetrabromo-1H-benzimidazole [DMAT] could partially disassemble the AIS of young neurons (Bréchet et al., 2008; Brachet et al., 2010), and tested the effect of DMAT treatment (3h at 20 µM) on the nanoscale organization of the mature AIS. In addition, we assessed the effect of increasing intracellular calcium concentration by incubating neurons in the presence of 45 mM KCl for 3 hours (Redmond et al., 2002). Increase in intracellular calcium concentration has been implicated in the AIS morphological plasticity (Grubb and Burrone, 2010a) and shown to trigger AIS disassembly in ischemic injury (Schafer et al., 2009). First, we measured the effect of these treatment on the overall morphology of the AIS at the diffraction-limited level (Fig. 7A-C): DMAT treatment did not alter the AIS concentration of ankG, and even elevated slightly the ßIV-spectrin labeling (Fig. 7D), without changing the length of the AIS (29.5 ± 0.6 µm for control, 27.9 ± 0.6 µm for DMAT, Fig. 7E), showing that mature neurons are resistant to acute CK2 inhibition. KCl treatment did result in partial disassembly of the AIS, with a ~30% drop in ßIV-spectrin and ankG labeling intensity (Fig. 7D) and a slight AIS shortening to 25.5 ± 0.5 µm (Fig. 7E).

STORM images of ßIV-spectrin SD were used to measure the effect of treatments on the AIS periodic lattice. Despite its absence of effect at the diffraction-limited level, we could detect a small drop in the ßIV-spectrin

bioRxiv preprint doi: https://doi.org/10.1101/022962; this version posted July 21, 2015. The copyright holder for this preprint (which was not certified by peer review) is the author/funder. All rights reserved. No reuse allowed without permission.

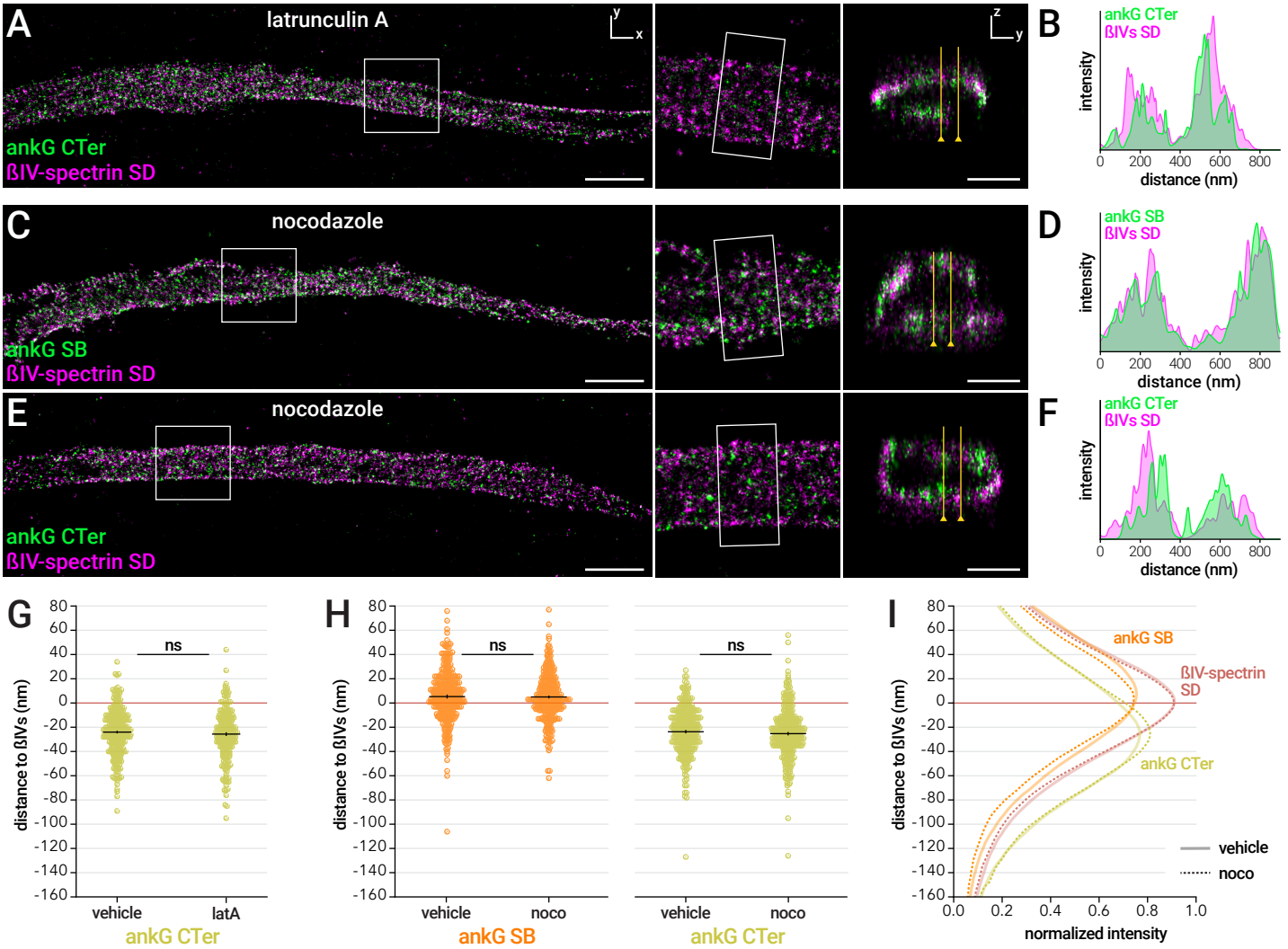

Figure 6. Radial orientation of ankG is resistant to actin or microtubule perturbation
(A-B) 3D-STORM images of the AIS from a neuron treated with latA (5 µM, 1h), fixed and labeled for ankG CTer (green) and ßIV-spectrin SD (magenta) (A). For (A), (C) and (E), scale bar is 2 µm for XY image, 0.5 µm for YZ section. Intensity profiles for each channel along the yellow line (B). (C-F) 3D-STORM image of the AIS from a neuron treated with nocodazole (20 µM, 3h), fixed and labeled for ankG SB (green) and ßIV-spectrin SD (magenta) (C), and corresponding intensity profiles (D). 3D-STORM image of the AIS from a neuron treated with nocodazole, fixed and labeled for ankG CTer (green) and ßIV-spectrin SD (magenta) (E), and corresponding intensity profiles (F). (G-H) Radial distance to ßIV-spectrin SD for the ankG CTer labeling in vehicle and latA-treated neurons (G, n=225-289 profiles, N=3). Radial distance to ßIV-spectrin SD for the ankG SB and CTer labeling in vehicle and nocodazole (noco) treated neurons (H, n=300-346, N=3-4). (I) Mean profiles for ßIV-spectrin SD (red), ankG SB (orange) and ankG CTer (yellow) treated with vehicle (plain) or nocodazole (dashed, mean ± SEM of average profiles, N=4-5).

periodicity of DMAT-treated neurons (Fig. 7F-G): the spacing distribution was similar (188 ± 7 nm for control, 187 ± 7 nm for DMAT, Fig. 7H), and the goodness of fit slightly dropped from 0.58 ± 0.01 to 0.51 ± 0.01 (Fig. 7I). KCl treatment had a stronger effect, with a flattened 189 ± 18 nm spacing distribution and a goodness of fit dropping at 0.27 ± 0.01. In contrast, DMAT and KCl treatments did not perturb the radial orientation of ankG (Fig. 7J-K), with an average distance of ankG CTer to ßIV-spectrin SD at -24 ± 1 nm, -27 ± 1 nm and -22 ± 2 nm for control, DMAT and KCl treatments, respectively (Fig 7L). In conclusion, the range of perturbation we performed (cytoskeleton, CK2 inhibition, intracellular calcium) showed that the AIS nano-architecture is robust, with alterations appearing only when significant disassembly occurs for the whole AIS.

Discussion

In this work, we have determined the nanoscale architecture of the AIS using super-resolution microscopy. STORM allowed us to quantitatively localize epitopes corresponding to known domains on AIS components, and infer the precise arrangement of the AIS scaffold. First, we directly demonstrated a ~190 nm periodic lattice along the AIS formed by actin rings connected by ßIV-spectrin dimers. Furthermore, we revealed the specific resistance of this ßIV-spectrin lattice against actin perturbation, compared to the ßII-spectrin lattice found along the distal axon. We characterized the yet unknown arrangement of the AIS master scaffolding protein, ankG: the aminoterminal part of ankG associates with membrane proteins and ßIV-spectrin, resulting in a similar periodic distribution. In contrast, the carboxyterminal part does not exhibit this periodicity: we explain this by demonstrating that the CTer of ankG localizes deeper in the axoplasm, below the submembrane lattice. We uncovered the overall radial orientation of ankG thanks to 3D STORM, and measured a ~32 nm distance between its SB and CTer domains. Moreover, this average radial extent is common to both the 480- and 270-kDa isoforms of ankG. Finally, we showed that the radial lattice periodicity, as well as the orientation of ankG, are resistant to a range of perturbations, revealing that this nanoscale organization is a robust and likely structural feature of the AIS.

bioRxiv preprint doi: https://doi.org/10.1101/022962; this version posted July 21, 2015. The copyright holder for this preprint (which was not certified by peer review) is the author/funder. All rights reserved. No reuse allowed without permission.

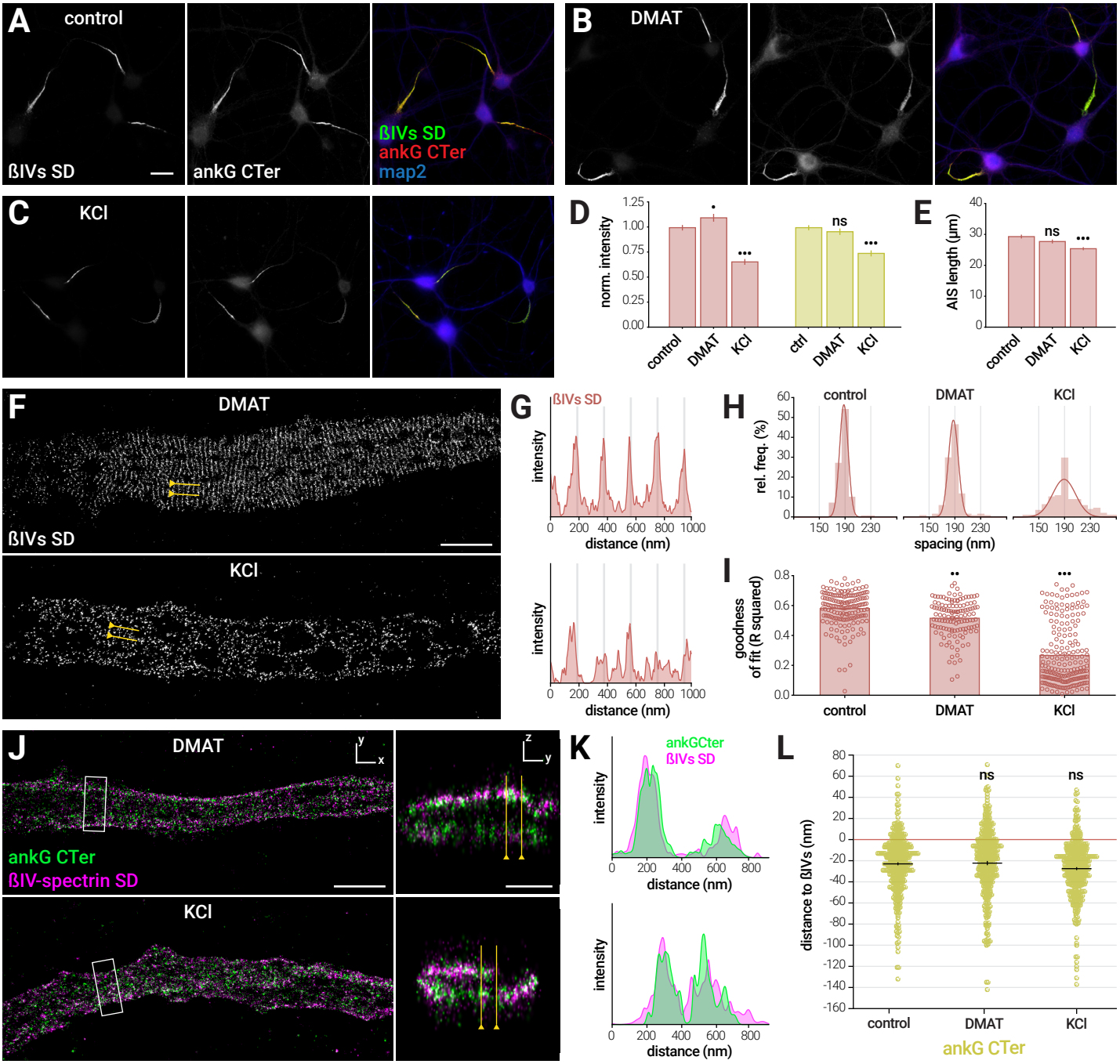

Figure 7. The AIS nano-architecture is partially altered by inhibition of CK2 or elevated intracellular calcium
(A-C) Sister cultures untreated (control, A), treated with the CK2 inhibitor DMAT (50 µM, 3h) (B), or incubated with 45 mM KCl for 3h (C), fixed and labeled for ßIV-spectrin (ßIVs SD, green), ankG CTer (red) and map2 (blue). Scale bar, 20 µm. (D-E) Immunolabeling intensity at the AIS for ßIV-spectrin SD (red, left) and ankG CTer (green, right), normalized to the control (ctrl) condition (D). AIS length measured on the ßIV-spectrin SD labeling (E, n=103-126 AIS, N=3-4). (F-G) STORM image of AIS from neurons treated with DMAT (top) or KCl (bottom), and labeled for ßIV-spectrin SD (F). Scale bar, 2 µm. Intensity profiles along the yellow lines (G). (H-I) Histogram of the spacing values in the control, DMAT and KCL conditions (H, n=130-206 profiles, N=3-4). Goodness of sinusoid fit (R squared) for the ßIV-spectrin SD labeling for control, DMAT or KCl treated neurons (I). (J-L) 3D-STORM images of the AIS from neurons treated with DMAT (top) or KCl (bottom), fixed and labeled for ankG CTer (green) and ßIV-spectrin SD (magenta) (J). Scale bar is 2 µm for XY image, 0.5 µm for YZ section. Intensity profiles for each channel along the yellow lines (K). Radial distance to ßIV-spectrin SD for the ankG CTer labeling in control, DMAT and KCl treated neurons (L, n=415-431, N=3-4).

Longitudinal organization: periodic submembrane actin/ ßIV-spectrin sheath

The first striking feature of the AIS nano-architecture is the periodic arrangement of its submembrane scaffold. We observed a regular distribution of actin every ~190 nm along the AIS, confirming the periodic actin rings recently described (Xu et al., 2013; D'Este et al., 2015). Furthermore, we found that both sides of ßIV-spectrin also organize as 190-nm spaced periodic bands, confirming recent reports (Xu et al., 2013; Zhong et al., 2014). Purified brain spectrin dimers have a length of ~195 nm (Bennett et al., 1982), suggesting a structural model where dimers of head-to-head ßIV-spectrin connect to actin rings at their NT extremities, and to ankG/Nav channels complexes near their central SD domain (see Fig. S2F). With 2-color STORM we could detect correlated bands for actin/ßIV-spectrin NT, and anti-correlated ones for actin/ßIV-spectrin SD, directly demonstrating the validity of this model. Interestingly, two

bioRxiv preprint doi: https://doi.org/10.1101/022962; this version posted July 21, 2015. The copyright holder for this preprint (which was not certified by peer review) is the author/funder. All rights reserved. No reuse allowed without permission.

isoforms of ßIV-spectrin exist at the AIS: the 270-kDa ßIV-spectrin Σ1, and the160-kDa ßIV-spectrin Σ6 that lacks the aminoterminal part of Σ1 (Komada and Soriano, 2002). ßIV-spectrin Σ1 binds both actin and ankG and is likely to form the basis of the ~190 nm periodic lattice, in contrast to the Σ6 isoform that does not bind actin. The detection of the two isoforms by the SD antibody could explain the higher localization counts, and the larger individual bands compared to the NT antibody that only recognize the Σ1 aminoterminus.

Recent work showed that a periodic lattice of ßII-spectrin first appears along the whole axon, before being replaced at the AIS by ßIV-spectrin (Zhong et al., 2014). This replacement is complete in the mature neurons we used, and furthermore we found the AIS ßIV-spectrin to be resistant to actin and microtubule perturbation, compared to the more distal ßII-spectrin lattice (Xu et al., 2013; Zhong et al., 2014). It is likely that in the AIS, the ßIV-spectrin/actin complex is stabilized by the ankG/Nav channels complex. In the distal axon, the periodic ßII-spectrin lattice does not depend on its ankyrin B partner (Lorenzo et al., 2014). Ankyrin B presence is required for ßII-spectrin preferential concentration into the axon (Zhong et al., 2014), supporting its function in axonal transport rather than membrane structure (Lorenzo et al., 2014).

Transverse organization: radial arrangement of ankG

The second striking feature of the AIS nano-architecture is the radial arrangement of ankG. We demonstrate that the carboxyterminal part of ankG departs from the submembrane periodic lattice, and is found deeper in the axoplasm. 3D-STORM and quantification of the radial distribution of epitopes allowed us to measure the radial extent of ankG, with a 32 nm average distance between the SB and CTer domains (see Fig. 4M). This radial orientation is likely to be functionally relevant, as it is observed for both the 270- and 480-kDa isoforms of ankG. AnkG could stretch to hundreds of nanometers if its tail was fully extended, so our 32 nm value indicates that it likely adopts convoluted conformations in the scaffold. Given the unstructured nature of the ankG tail (Bennett and Lorenzo, 2013), it is likely that our obtained value averages a large number of dynamic conformations, analogous to the radius of gyration for a flexible polymer.

Role of ankG in regulating protein transport trough the AIS

The "dendrification" of the proximal axon observed after ankG depletion (Hedstrom et al., 2008; Sobotzik et al., 2009) led to propose a role for the AIS in the maintenance of axonal identity (Rasband, 2010). This is thought to occur via two cellular mechanisms: a diffusion barrier that restrict membrane protein and lipid diffusion along the AIS surface, and an intracellular filter that regulates protein diffusion and transport to and from the axon (Leterrier and Dargent, 2014). Since its initial description (Song et al., 2009), the existence of an intracellular filter in the AIS that regulates protein traffic between the soma and axon is still a debated issue (Petersen et al., 2014; Watanabe et al., 2012). Its molecular mechanism, in particular how ankG could participate in the regulation of protein transport into the axon remains unknown. AnkG has been primarily detected near the plasma membrane by immunogold EM (Iwakura et al., 2012; Le Bras et al., 2013). Our results show that indeed, reached depth of radially-oriented ankG is within 50 nanometers from the plasma membrane. However, ankG can bind microtubules via EB1/3 proteins (Leterrier et al., 2011), and the proximal axon of ankG-deficient neurons is devoid of the characteristic microtubule fascicles (Sobotzik et al., 2009). Together with our structural results, this suggests that the ankG-based scaffold could spatially organize microtubules close to the axolemma in the AIS, and this could in turn have an influence on polarized traffic. Interestingly, a recently identified giant ankG isoform organizes the spatial distribution of microtubules along the axonal shaft in Drosophila neurons (Stephan et al., 2015).

We tested the robustness of the AIS nano-architecture using a range of cytoskeletal and pharmacological perturbations. The periodic ßIV-spectrin lattice was resistant to actin and microtubule perturbation, in contrast to the ßII-spectrin lattice found along the distal axon that is depends on actin and partially on microtubules (Zhong et al., 2014). The radial orientation of ankG in the AIS was similarly resistant to cytoskeleton perturbations. Moreover, short-term treatments aimed at destabilizing the AIS (CK2 inhibitor, high KCl concentration) could alter the ßIV-spectrin periodic lattice or the radial orientation of ankG, but only in situations where the whole AIS was undergoing significant disassembly. This suggests that these nanoscale features of the AIS scaffold are structural and essential for the stability of the AIS as a compartment.

The AIS, from cellular traffic to brain and nervous system disorders

In conclusion, we show that the AIS scaffold is a precisely organized compartment, with a longitudinal periodicity and a radial layering. This nanoscale organization is robust, pointing to its potential importance for proper cell function. Our work confirms the strength of super-resolution microscopy for elucidating the architecture of neuronal assemblies, down to the macromolecular level (Maglione and Sigrist, 2013). Knowledge of the AIS nanoscale architecture will help deciphering the molecular mechanisms that underpin neuronal excitability and protein mobility in polarized cells. Beyond this fundamental relevance, understanding the AIS structure and function has neuro-pathological implications. AnkG gene variants and mutations have been consistently associated with in several neuropsychiatric disorders, including bipolar disorders and schizophrenia (Iqbal et al., 2013; Leussis et al., 2012). Furthermore, affected axonal transport is a key factor in most neurodegenerative diseases, and the gatekeeper function of the AIS could be implicated (Sun et al., 2014). Our structural work will hopefully open the way to a better understanding of the AIS crucial functions, in physiological as well as pathological contexts.

Materials and Methods

Antibodies, plasmids and reagents

Rabbit polyclonal anti ßIV-spectrin antibodies were gifts from Matthew Rasband (Baylor College of Medicine, Austin, TX). Rabbit polyclonal anti 480-kDa ankG (residues 3516-3530 of human 480-kDa ankG) was a gift from François Couraud (Université Pierre et Marie Curie, Paris). For two-color STORM, paired fluorophore-conjugated secondary antibodies were made by coupling unconjugated antibodies with reactive activator and reporter fluorophores, according to the N-STORM sample preparation protocol (Nikon Instruments).

Animals and neuronal cultures

The use of Wistar rats followed the guidelines established by the European Animal Care and Use Committee (86/609/CEE) and was approved by the local ethics committee (agreement D13-055-8). Rat hippocampal neurons were cultured on 18 mm coverslips at a density of 6,000/cm2 following the Banker method, above a feeder glia layer in B27-supplemented medium (Kaech and Banker, 2006).

Immunocytochemistry and STORM imaging

After 14 to 21 days in culture, neurons were fixed using 4% PFA or using an extraction-fixation method optimized for microtubule labeling (Yau et al., 2014). After blocking, they were incubated with primary antibodies overnight at 4°C, then with secondary antibodies for 1h at room temperature. STORM imaging was performed on an N-STORM microscope

bioRxiv preprint doi: https://doi.org/10.1101/022962; this version posted July 21, 2015. The copyright holder for this preprint (which was not certified by peer review) is the author/funder. All rights reserved. No reuse allowed without permission.

(Nikon Instruments). Coverslips were imaged in STORM buffer: Tris 50 mM pH 8, NaCl 10 mM, 10% glucose, 100 mM MEA, 0.56 mg/mL glucose oxidase (or alternatively 3.5 U/mL pyranose oxidase), 40 µg/mL catalase. For single color imaging, the sample was continuously illuminated at 647 nm (full power) and a 30,000-60,000 images were acquired at 67 Hz, with progressive reactivation by simultaneous 405 nm illumination. Two-color STORM imaging was either performed by successive imaging with 488 and 647 nm lasers (for double staining with phalloidin-Atto 488, Nanguneri et al., 2014), or using two sequences of one activator frame followed by three reporter frames (for double immunolabeling, Bates et al., 2007). The N-STORM software (Nikon Instruments) was used for the localization of single fluorophore activations.

Image Processing and analysis

Image reconstructions were performed using the ThunderSTORM ImageJ plugin (Ovesny et al., 2014) in Fiji software (Schindelin et al., 2012). Custom scripts and macros were used to automate images reconstructions. For quantification of longitudinal periodicities, intensity profiles were drawn on 4 nm/pixel reconstructions and fitted using a sinusoid function. The histogram of spacing values was fitted with a Gaussian curve to obtain the mean spacing and spread. For quantification of radial distributions, line profiles were drawn on YZ transverse projections, and the distance between epitopes defined as the difference between the maxima of Gaussian fits on each channel. For mean profile graphs (Figure 4L and 6I), profiles were aligned using the ßIV-spectrin SD channel, and averaged across profiles. For quantification of the AIS position on epifluorescence images, a line profile was drawn along the axon, starting at the emergence point from the soma. The begin and end of the AIS were defined as the position along the smoothed profile where intensity first rose above 35% and last dropped below 10% of the maximum intensity value, respectively (Grubb and Burrone, 2010b).

Acknowledgments

We thank M. Rasband, V. Bennett and F. Couraud for providing antibodies and plasmids. We also would like to thank D. Choquet and J-B Sibarita for insightful discussions; D. Marguet, S. Mailfert and M. Mondin for their help during the initial stages of this study; S. Bezin at Nikon Instruments and M.-P. Blanchard at CRN2M imaging facility for their assistance; F. Castets and M.-J. Papandreou for discussions and careful reading of the manuscript.

Author contributions

CL: conception and design, acquisition of data, analysis and interpretation of data, drafting or revising the article. JP: acquisition of data, analysis and interpretation of data. GC: acquisition of data. FRB: contributed essential data or reagents. BD: conception and design, interpretation of data, drafting or revising the article. This work was supported by a grant to BD from the French Agence Nationale de la Recherche (ANR-2011-BSV4-001-1). The authors declare that no competing interests exist.

References

Bates, M., B. Huang, G.T. Dempsey, and X. Zhuang. 2007. Multicolor super-resolution imaging with photo-switchable fluorescent probes. Science. 317:1749–1753. doi:10.1126/science.1146598.

Bennett, V., and D.N. Lorenzo. 2013. Spectrin- and ankyrin-based membrane domains and the evolution of vertebrates. Curr Top Membr. 72:1–37. doi:10.1016/B978-0-12-417027-8.00001-5.

Bennett, V., J.Q. Davis, and W.E. Fowler. 1982. Brain spectrin, a membrane-associated protein related in structure and function to erythrocyte spectrin. Nature. 299:126–131.

Brachet, A., C. Leterrier, M. Irondelle, M.-P. Fache, V. Racine, J.-B. Sibarita, D. Choquet, and B. Dargent. 2010. Ankyrin G restricts ion channel diffusion at the axonal initial segment before the establishment of the diffusion barrier. J. Cell Biol. 191:383–395. doi:10.1083/jcb.201003042.

Bréchet, A., M.-P. Fache, A. Brachet, G. Ferracci, A. Baude, M. Irondelle, S. Pereira, C. Leterrier, and B. Dargent. 2008. Protein kinase CK2 contributes to the organization of sodium channels in axonal membranes by regulating their interactions with ankyrin G. J. Cell Biol. 183:1101–1114. doi:10.1083/jcb.200805169.

D'Este, E., D. Kamin, F. Göttfert, A. El-Hady, and S.W. Hell. 2015. STED nanoscopy reveals the ubiquity of subcortical cytoskeleton periodicity in living neurons. Cell Rep. 10:1246–1251. doi:10.1016/j.celrep.2015.02.007.

Galiano, M.R., S. Jha, T.S.-Y. Ho, C. Zhang, Y. Ogawa, K.-J. Chang, M.C. Stankewich, P.J. Mohler, and M.N. Rasband. 2012. A distal axonal cytoskeleton forms an intra-axonal boundary that controls axon initial segment assembly. Cell. 149:1125–1139. doi:10.1016/j.cell.2012.03.039.

Grubb, M.S., and J. Burrone. 2010a. Activity-dependent relocation of the axon initial segment fine-tunes neuronal excitability. Nature. 465:1070–1074. doi:10.1038/nature09160.

Grubb, M.S., and J. Burrone. 2010b. Building and maintaining the axon initial segment. Curr. Opin. Neurobiol. 20:481–488. doi:10.1016/j.conb.2010.04.012.

Hedstrom, K., X. Xu, Y. Ogawa, R. Frischknecht, C. Seidenbecher, P. Shrager, and M.N. Rasband. 2007. Neurofascin assembles a specialized extracellular matrix at the axon initial segment. J. Cell Biol. 178:875–886.

Hedstrom, K., Y. Ogawa, and M.N. Rasband. 2008. AnkyrinG is required for maintenance of the axon initial segment and neuronal polarity. J. Cell Biol. 183:635–640.

Hsu, W.-C.J., C.L. Nilsson, and F. Laezza. 2014. Role of the axonal initial segment in psychiatric disorders: function, dysfunction, and intervention. Front Psychiatry. 5:109. doi:10.3389/fpsyt.2014.00109.

Huang, B., W. Wang, M. Bates, and X. Zhuang. 2008. Three-dimensional super-resolution imaging by stochastic optical reconstruction microscopy. Science. 319:810–813. doi:10.1126/science.1153529.

Iqbal, Z., G. Vandeweyer, M. van der Voet, A.M. Waryah, M.Y. Zahoor, J.A. Besseling, L.T. Roca, A.T. Vulto-van Silfhout, B. Nijhof, J.M. Kramer, N. Van der Aa, M. Ansar, H. Peeters, C. Helsmoortel, C. Gilissen, L.E.L.M. Vissers, J.A. Veltman, A.P.M. de Brouwer, R. Frank Kooy, S. Riazuddin, A. Schenck, H. van Bokhoven, and L. Rooms. 2013. Homozygous and heterozygous disruptions of ANK3: at the crossroads of neurodevelopmental and psychiatric disorders. Hum. Mol. Genet. 22:1960–1970. doi:10.1093/hmg/ddt043.

Iwakura, A., M. Uchigashima, T. Miyazaki, M. Yamasaki, and M. Watanabe. 2012. Lack of molecular-anatomical evidence for GABAergic influence on axon initial segment of cerebellar purkinje cells by the pinceau formation. J. Neurosci. 32:9438–9448. doi:10.1523/JNEUROSCI.1651-12.2012.

Jaworski, J., L.C. Kapitein, S.M. Gouveia, B.R. Dortland, P.S. Wulf, I. Grigoriev, P. Camera, S.A. Spangler, P. Di Stefano, J. Demmers, H.J. Krugers, P. Defilippi, A. Akhmanova, and C.C. Hoogenraad. 2009. Dynamic microtubules regulate dendritic spine morphology and synaptic plasticity. Neuron. 61:85–100. doi:10.1016/j.neuron.2008.11.013.

Jenkins, P.M., N. Kim, S.L. Jones, W.-C. Tseng, T.M. Svitkina, H.H. Yin, and V. Bennett. 2015. Giant ankyrin-G: a critical innovation in vertebrate evolution of fast and integrated neuronal signaling. Proc. Natl. Acad. Sci. U.S.A. 112:957–964. doi:10.1073/pnas.1416544112.

Jenkins, S.M., and V. Bennett. 2001. Ankyrin-G coordinates assembly of the spectrin-based membrane skeleton, voltage-gated sodium channels, and L1 CAMs at Purkinje neuron initial segments. J. Cell Biol. 155:739–746. doi:10.1083/jcb.200109026.

Jones, S.L., F. Korobova, and T. Svitkina. 2014. Axon initial segment cytoskeleton comprises a multiprotein submembranous coat containing sparse actin filaments. J. Cell Biol. 2:89. doi:10.1016/j.neuron.2011.02.021.

Kaech, S., and G.A. Banker. 2006. Culturing hippocampal neurons. Nat. Protoc. 1:2406–2415.

Kapitein, L.C., and C.C. Hoogenraad. 2011. Which way to go? Cytoskeletal organization and polarized transport in neurons. Mol. Cell. Neurosci. 46:9–20. doi:10.1016/j.m

Maglione, M., and S.J. Sigrist. 2013. Seeing the forest tree by tree: super-resolution light microscopy meets the neurosciences. Nat. Neurosci. 16:790–797. doi:10.1038/nn.3403.

Nakada, C., K. Ritchie, Y. Oba, M. Nakamura, Y. Hotta, R. Iino, R. Kasai, K. Yamaguchi, T.K. Fujiwara, and A. Kusumi. 2003. Accumulation of anchored proteins forms membrane diffusion barriers during neuronal polarization. Nat. Cell Biol. 5:626–632.

Nanguneri, S., B. Flottmann, F. Herrmannsdörfer, T. Kuner, and M. Heilemann. 2014. Single-molecule super-resolution imaging by tryptophcn.2010.08.015.

Komada, M., and P. Soriano. 2002. [Beta]IV-spectrin regulates sodium channel clustering through ankyrin-G at axon initial segments and nodes of Ranvier. J. Cell Biol. 156:337–348. doi:10.1083/jcb.200110003.

Le Bras, B., A. Fréal, A. Czarnecki, P. Legendre, E. Bullier, M. Komada, P.J. Brophy, M. Davenne, and F. Couraud. 2013. In vivo assembly of the axon initial segment in motor neurons. Brain Struct Funct. doi:10.1007/s00429-013-0578-7.

Leterrier, C., and B. Dargent. 2014. No Pasaran! Role of the axon initial segment in the regulation of protein transport and the maintenance of axonal identity. Semin. Cell Dev. Biol. 27C:44–51. doi:10.1016/j.semcdb.2013.11.001.

Leterrier, C., H. Vacher, M.-P. Fache, S. Angles d'Ortoli, F. Castets, A. Autillo-Touati, and B. Dargent. 2011. End-binding proteins EB3 and EB1 link microtubules to ankyrin G in the axon initial segment. Proc. Natl. Acad. Sci. U.S.A. 108:8826–8831. doi:10.1073/pnas.1018671108.

Leussis, M.P., J.M. Madison, and T.L. Petryshen. 2012. Ankyrin 3: genetic association with bipolar disorder and relevance to disease pathophysiology. Biol Mood Anxiety Disord. 2:18. doi:10.1186/2045-5380-2-18.

Lorenzo, D.N., A. Badea, J.Q. Davis, J. Hostettler, J. He, G. Zhong, X. Zhuang, and V. Bennett. 2014. A PIK3C3-Ankyrin-B-Dynactin pathway promotes axonal growth and multiorganelle transport. J. Cell Biol. 207:735–752. doi:10.1083/jcb.201407063.an-quenching-induced

bioRxiv preprint doi: https://doi.org/10.1101/022962; this version posted July 21, 2015. The copyright holder for this preprint (which was not certified by peer review) is the author/funder. All rights reserved. No reuse allowed without permission.

photoswitching of phalloidin-fluorophore conjugates. Microsc. Res. Tech. 77:510–516. doi:10.1002/jemt.22349.

Normand, E.A., and M.N. Rasband. 2015. Subcellular patterning: axonal domains with specialized structure and function. Dev. Cell. 32:459–468. doi:10.1016/j.devcel.2015.01.017.

Ovesny, M., P. Křížek, J. Borkovec, Z. Svindrych, and G.M. Hagen. 2014. ThunderSTORM: a comprehensive ImageJ plug-in for PALM and STORM data analysis and super-resolution imaging. Bioinformatics. 30:2389–2390. doi:10.1093/bioinformatics/btu202.

Petersen, J.D., S. Kaech, and G.A. Banker. 2014. Selective microtubule-based transport of dendritic membrane proteins arises in concert with axon specification. J. Neurosci. 34:4135–4147. doi:10.1523/JNEUROSCI.3779-13.2014.

Rasband, M.N. 2010. The axon initial segment and the maintenance of neuronal polarity. Nat. Rev. Neurosci. 11:552–562. doi:10.1038/nrn2852.

Redmond, L., A.H. Kashani, and A. Ghosh. 2002. Calcium regulation of dendritic growth via CaM kinase IV and CREB-mediated transcription. Neuron. 34:999–1010.

Schafer, D.P., S. Jha, F. Liu, T. Akella, L.D. McCullough, and M.N. Rasband. 2009. Disruption of the axon initial segment cytoskeleton is a new mechanism for neuronal injury. J. Neurosci. 29:13242–13254. doi:10.1523/JNEUROSCI.3376-09.2009.

Schindelin, J., I. Arganda-Carreras, E. Frise, V. Kaynig, M. Longair, T. Pietzsch, S. Preibisch, C. Rueden, S. Saalfeld, B. Schmid, J.-Y. Tinevez, D.J. White, V. Hartenstein, K.W. Eliceiri, P. Tomancak, and A. Cardona. 2012. Fiji: an open-source platform for biological-image analysis. Nat. Methods. 9:676–682. doi:10.1038/nmeth.2019.

Sobotzik, J.-M., J.M. Sie, C. Politi, D. Del Turco, V. Bennett, T. Deller, and C. Schultz. 2009. AnkyrinG is required to maintain axo-dendritic polarity in vivo. Proc. Natl. Acad. Sci. U.S.A. 106:17564–17569. doi:10.1073/pnas.0909267106.

Song, A.-H., D. Wang, G. Chen, Y. Li, J. Luo, S. Duan, and M.-M. Poo. 2009. A selective filter for cytoplasmic transport at the axon initial segment. Cell. 136:1148–1160. doi:10.1016/j.cell.2009.01.016.

Stephan, R., B. Goellner, E. Moreno, C.A. Frank, T. Hugenschmidt, C. Genoud, H. Aberle, and J. Pielage. 2015. Hierarchical microtubule organization controls axon caliber and transport and determines synaptic structure and stability. Dev. Cell. 33:5–21. doi:10.1016/j.devcel.2015.02.003.

Sun, X., Y. Wu, M. Gu, Z. Liu, Y. Ma, J. Li, and Y. Zhang. 2014. Selective filtering defect at the axon initial segment in Alzheimer's disease mouse models. Proc. Natl. Acad. Sci. U.S.A. doi:10.1073/pnas.1411837111.

Watanabe, K., S. Al-Bassam, Y. Miyazaki, T.J. Wandless, P. Webster, and D.B. Arnold. 2012. Networks of polarized actin filaments in the axon initial segment provide a mechanism for sorting axonal and dendritic proteins. Cell Rep. 2:1546–1553. doi:10.1016/j.celrep.2012.11.015.

Winckler, B., P. Forscher, and I. Mellman. 1999. A diffusion barrier maintains distribution of membrane proteins in polarized neurons. Nature. 397:698–701.

Xu, K., G. Zhong, and X. Zhuang. 2013. Actin, spectrin, and associated proteins form a periodic cytoskeletal structure in axons. Science. 339:452–456. doi:10.1126/science.1232251.

Yang, Y., Y. Ogawa, K. Hedstrom, and M.N. Rasband. 2007. betaIV spectrin is recruited to axon initial segments and nodes of Ranvier by ankyrinG. J. Cell Biol. 176:509–519.

Yau, K.W., S.F.B. van Beuningen, I. Cunha-Ferreira, B.M.C. Cloin, E.Y. van Battum, L. Will, P. Schätzle, R.P. Tas, J. van Krugten, E.A. Katrukha, K. Jiang, P.S. Wulf, M. Mikhaylova, M. Harterink, R.J. Pasterkamp, A. Akhmanova, L.C. Kapitein, and C.C. Hoogenraad. 2014. Microtubule Minus-End BindingProtein CAMSAP2 Controls Axon Specification and Dendrite Development. Neuron. 82:1058–1073. doi:10.1016/j.neuron.2014.04.019.

Zhang, X., and V. Bennett. 1998. Restriction of 480/270-kD ankyrin G to axon proximal segments requires multiple ankyrin G-specific domains. J. Cell Biol. 142:1571–1581.

Zhong, G., J. He, R. Zhou, D. Lorenzo, H.P. Babcock, V. Bennett, and X. Zhuang. 2014. Developmental mechanism of the periodic membrane skeleton in axons. Elife. 3. doi:10.7554/eLife.04581.

Supplementary Figures

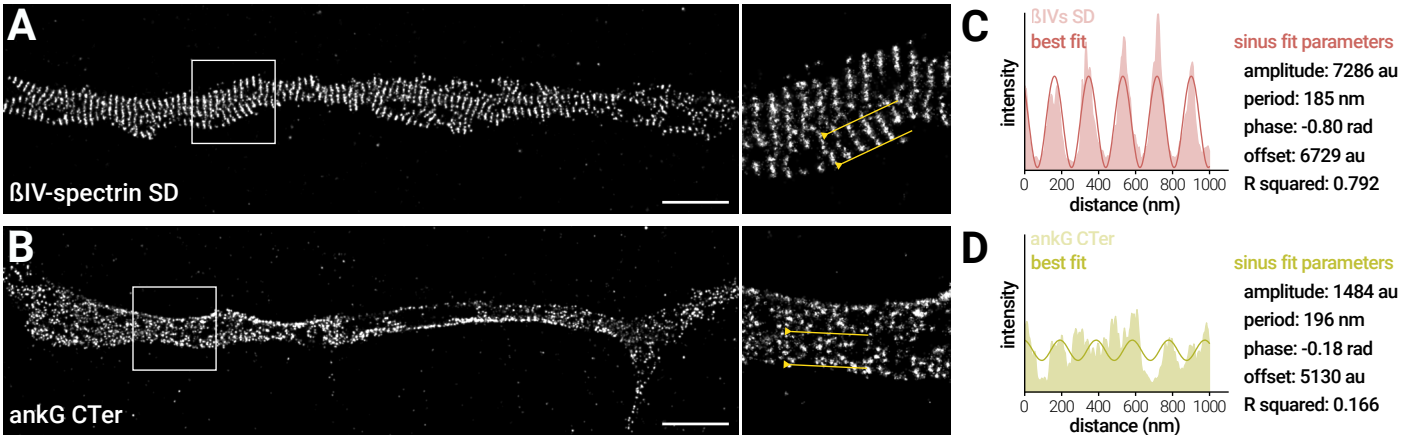

Figure S1. Quantification of STORM images: labeling periodicity
(A-D) Quantification of the labeling periodicity on STORM images. (A-B) STORM image of an AIS with a highly periodic labeling (ßIV-spectrin SD) (A). For (A) and (C), scale bar is 2 µm. Intensity profile along the yellow line (B, light red). Red curve is the sinusoid fitted on the profile, with fitted parameters given on the right. (C-D) AIS with a low periodicity labeling (ankG CTer) (C), and corresponding intensity profile (D, light green). Green curve is the sinusoid fitted on the profile, with fitted parameters given on the right.

bioRxiv preprint doi: https://doi.org/10.1101/022962; this version posted July 21, 2015. The copyright holder for this preprint (which was not certified by peer review) is the author/funder. All rights reserved. No reuse allowed without permission.

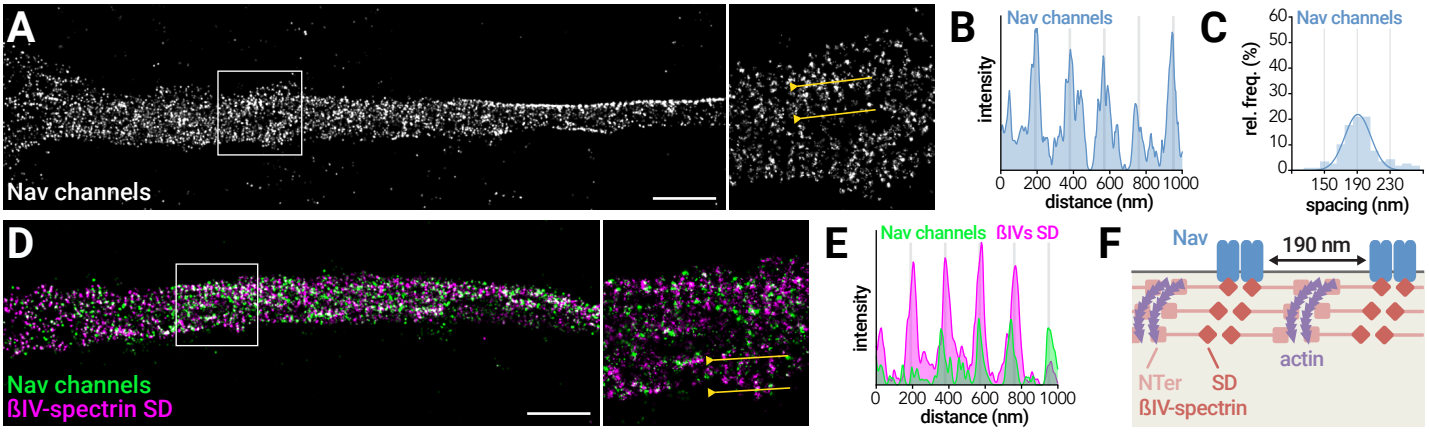

Figure S2. Nav channels are organized along the ßIV-spectrin periodic lattice
(A-C) STORM image of an AIS labeled for Nav channels (A). For (A) and (D), scale bar is 2 µm. Intensity profile along the yellow line (B), and histogram of the spacing values (C, n=120 profiles, N=3). (D-E) 2-color STORM image of an AIS labeled for Nav channels (green) and ßIV-spectrin SD (magenta) (D), and corresponding intensity profiles (E). (F) Structural model of the sub-membrane actin/ßIV-spectrin lattice.

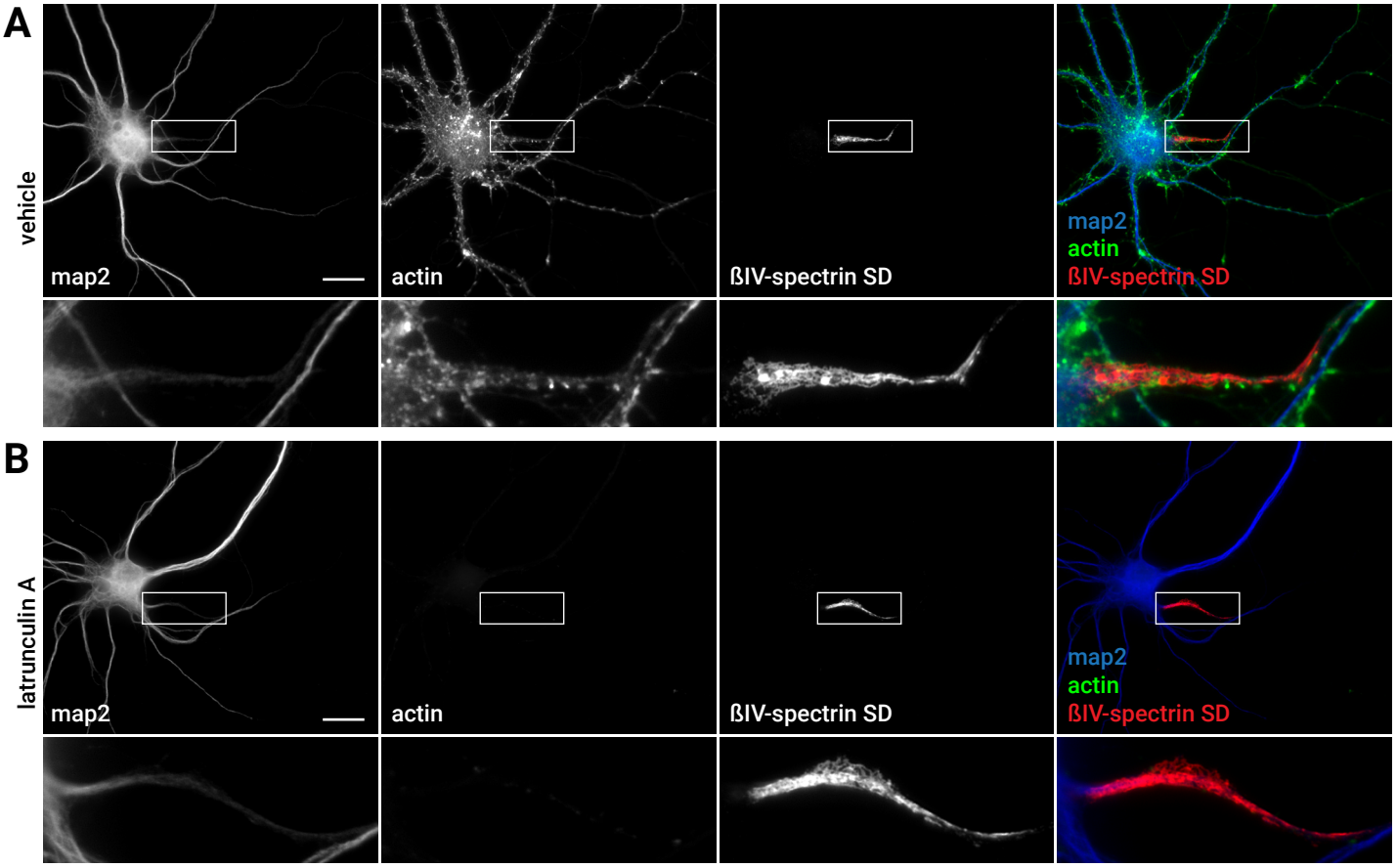

Figure S3. Effect of latA on actin and ßIV-spectrin diffraction-limited labeling
(A-B) Widefield epifluorescence image of a 16 div neuron treated with vehicle (DMSO 0.1%, 1h)(A) or latA (5 µM, 1h)(B), fixed and labeled for map2 (blue on overlay), actin (green on overlay), and ßIV-spectrin SD (red on ov erlay). Scale bars, 20 µm.

bioRxiv preprint doi: https://doi.org/10.1101/022962; this version posted July 21, 2015. The copyright holder for this preprint (which was not certified by peer review) is the author/funder. All rights reserved. No reuse allowed without permission.

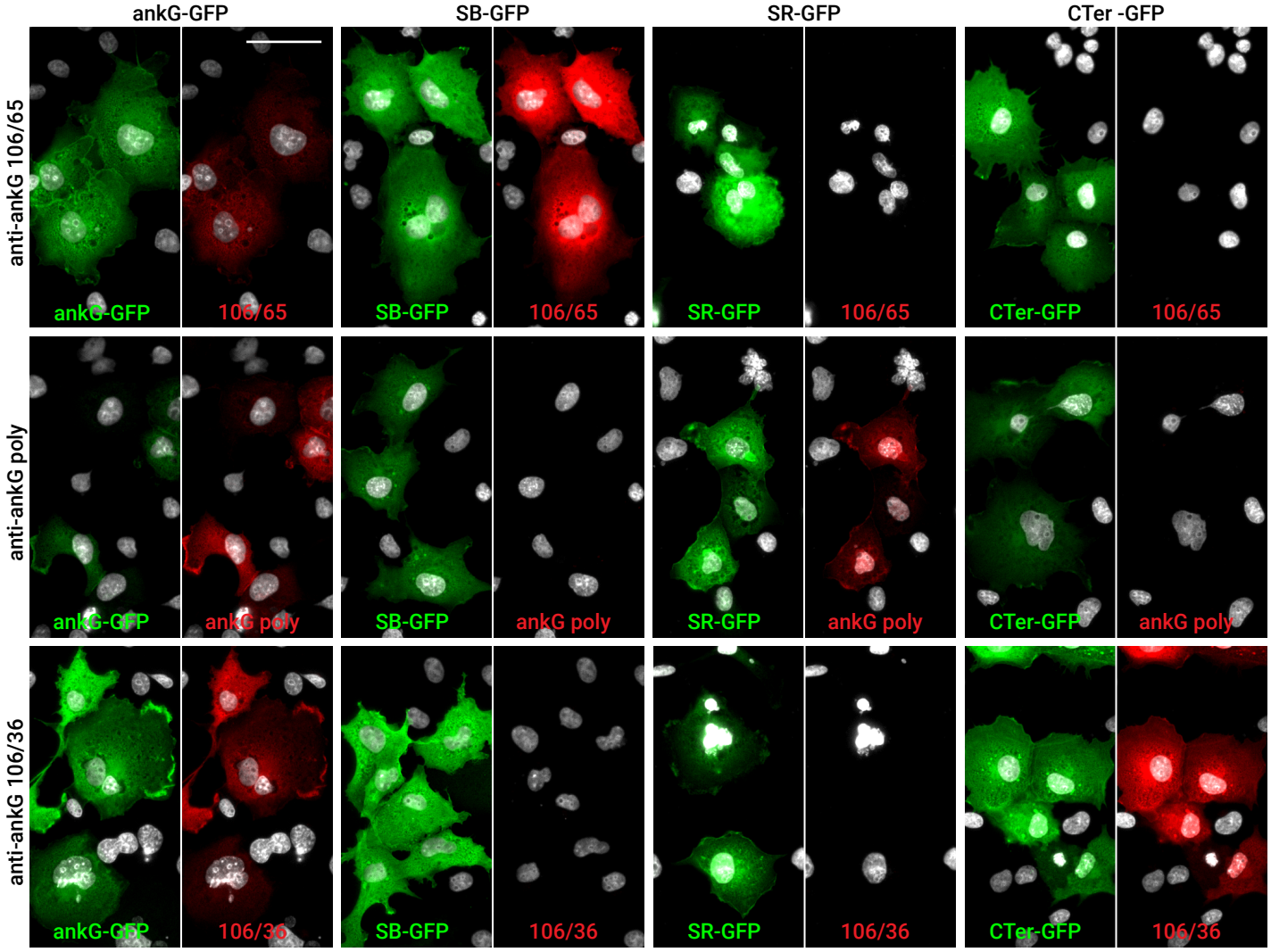

Figure S4. Determination of the target domains for the anti-ankG antibodies
COS cells expressing 270-kDa ankG-GFP or different isolated ankG domains fused to GFP (columns, green), labeled using one of three anti-ankG antibodies (rows, red). All antibodies recognize the full-length ankG-GFP, the 106/65 antibody recognizes the SB domain, the polyclonal antibody recognizes the SR domain, and the 106/36 antibody recognizes the CTer domain. Scale bar, 50 µm.

bioRxiv preprint doi: https://doi.org/10.1101/022962; this version posted July 21, 2015. The copyright holder for this preprint (which was not certified by peer review) is the author/funder. All rights reserved. No reuse allowed without permission.

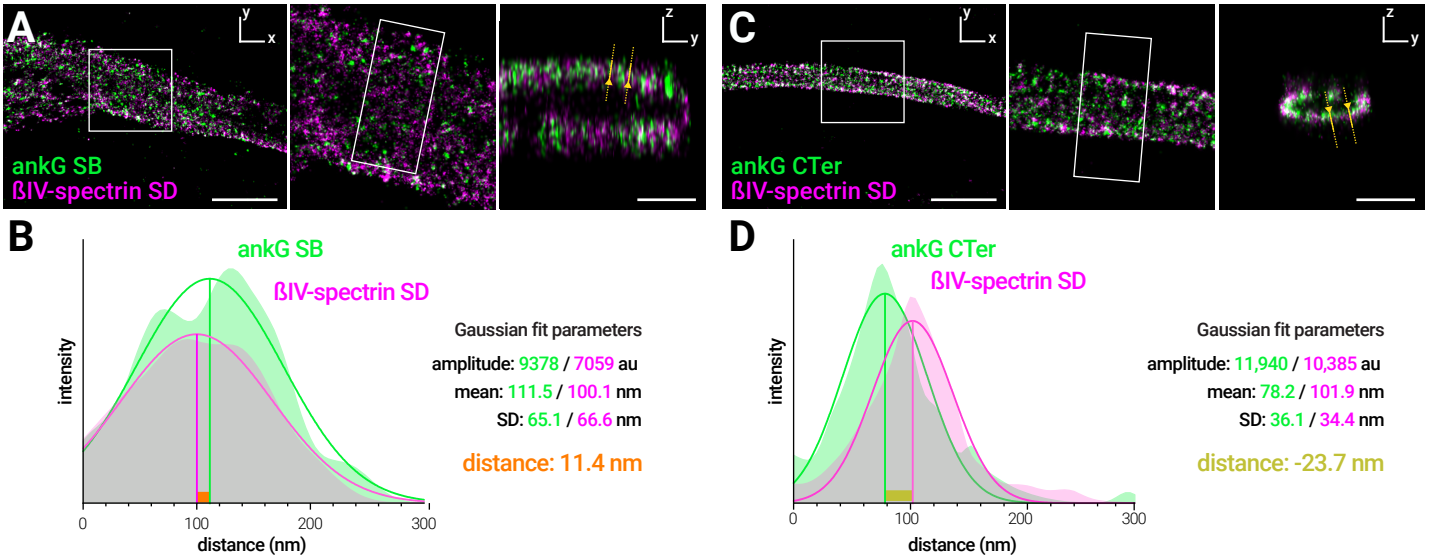

Figure S5. Quantification of the radial labeling organization
(A-B) STORM image of an AIS labeled for ankG SB (green) and ßIV-spectrin SD (magenta) (A). For (A) and (C), scale bar is 2 µm on XY image, 0.5 µm on YZ section. Intensity profiles for each channel along the yellow line (B). Green and magenta curves are Gaussian fit of the ankG SB and ßIV-spectrin SD profiles, respectively. Positive distance indicates that the ankG SB labeling localizes at the periphery of the ßIV-spectrin SD labeling. (C-D) AIS labeled for ankG CTer (green) and ßIV-spectrin SD (magenta) (C), and corresponding intensity profiles (D). Negative distance indicates that the ankG CTer labeling is found inside the ßIV-spectrin SD labeling.

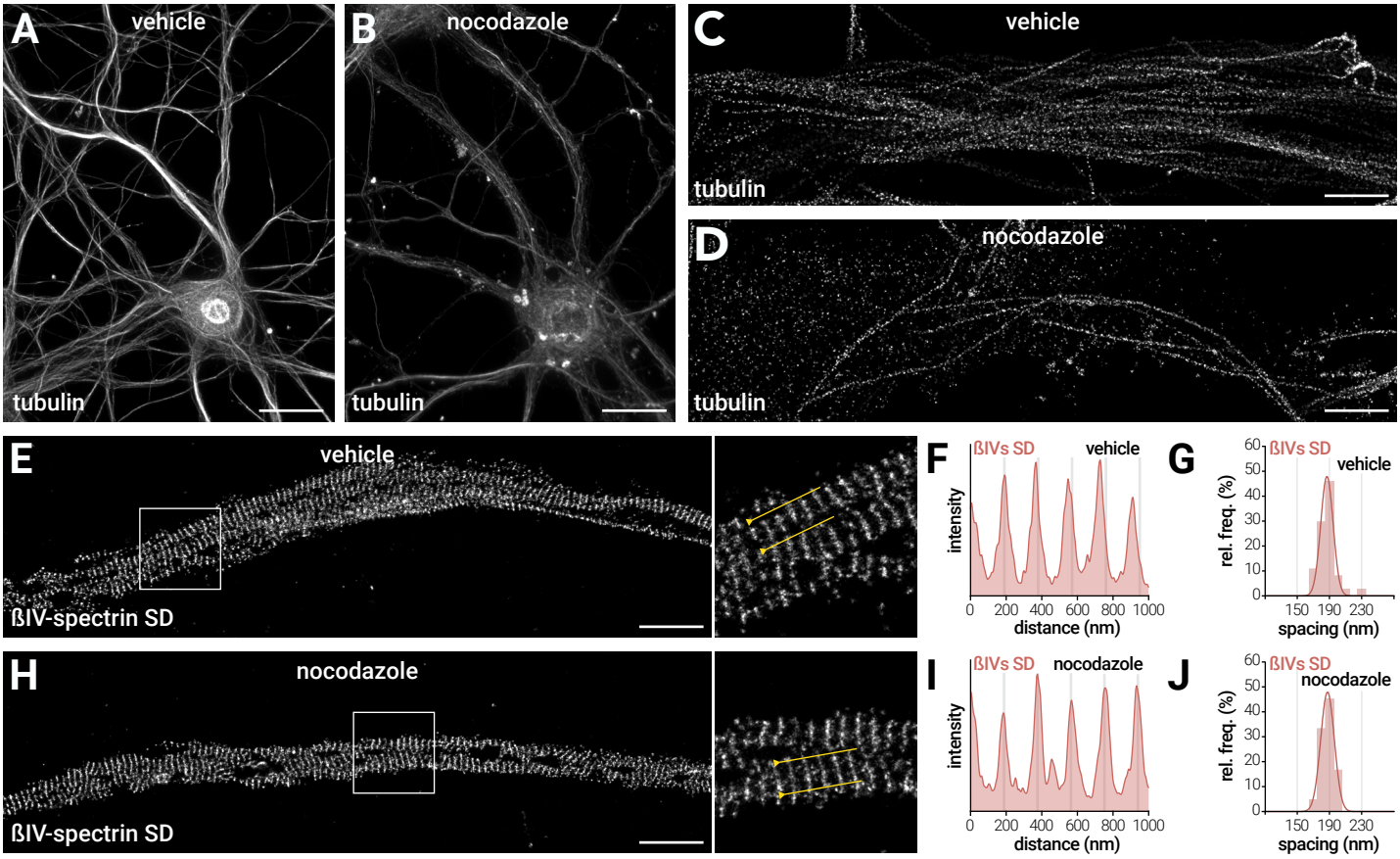

Figure S6. Effect of nocodazole on microtubules and ßIV-spectrin SD distribution
(A-B) Deconvolved epifluorescence image of neurons treated with vehicle (DMSO 0.1%, 5h) (A) or nocodazole (20 µM, 3h) (B), extracted/fixed and stained for microtubules (α-tubulin). Scale bars, 20 µm. (C-D) STORM image of an AIS from a neuron treated with vehicle (A) or nocodazole (D), extracted/fixed and stained for α-tubulin. Scale bars, 2 µm. (E-G) AIS of a neuron treated with vehicle, fixed and stained for ßIV-spectrin SD (E). For (E) and (H), scale bar is 2 µm. Intensity profile along the yellow line (F), and histogram of the spacing values (veh, n=37 profiles, N=2). (H-J) AIS of a neuron from a sister coverslip treated with nocodazole, fixed and stained for ßIV-spectrin SD (H), corresponding intensity profile (I), and histogram of the spacing values (noco, n=42, N=2).

bioRxiv preprint doi: https://doi.org/10.1101/022962; this version posted July 21, 2015. The copyright holder for this preprint (which was not certified by peer review) is the author/funder. All rights reserved. No reuse allowed without permission.

Labeling	Mean spacing (nm)	Spread (nm)	R squared
Figure 1. Actin and longitudinal ßIV-spectrin dimers form the AIS periodic submembrane lattice			
actin *	188.0 ± 0.2	8.3 ± 0.2	0.39 ± 0.02
ßIVs NT	191.0 ± 0.1	6.8 ± 0.1	0.55 ± 0.01
ßIVs SD	187.8 ± 0.1	7.5 ± 0.1	0.57 ± 0.01
Figure S2. Nav channels are organized along the ßIV-spectrin periodic lattice			
Nav	190.3 ± 1.0	15.9 ± 1.0	0.25 ± 0.01
Figure 2. The AIS submembrane lattice is resistant to actin perturbation			
actin (veh) *	188.0 ± 0.2	8.3 ± 0.2	0.39 ± 0.02
actin (latA)	184.0 ± 1.2	13.3 ± 1.2	0.21 ± 0.01
ßIVs SD (veh)	188.1 ± 0.1	8.0 ± 0.1	0.63 ± 0.01
ßIVs SD (latA)	189.6 ± 0.1	6.8 ± 0.1	0.64 ± 0.01
ßIIs CTer (veh)	188.3 ± 0.5	8.3 ± 0.4	0.54 ± 0.01
ßIIs CTer (latA)	179.1 ± 2.1	21.6 ± 2.1	0.25 ± 0.01
Figure 3. AnkG associates with the periodic spectrin lattice, but becomes disordered away from the spectrin binding site			
ankG SB	187.7 ± 0.6	13.5 ± 0.6	0.34 ± 0.01
ankG SR	187.6 ± 0.9	14.1 ± 0.9	0.26 ± 0.01
ankG CTer	183.7 ± 1.1	20.3 ± 1.1	0.22 ± 0.01
Figure 5. The 270- and 480-kDa isoforms of ankG have a similar radial extent			
ankG CTer	183.7 ± 1.1	20.3 ± 1.1	0.22 ± 0.01
ankG tail480	182.2 ± 4.1	26.9 ± 4.1	0.20 ± 0.01
Figure S5. Effect of nocodazole on microtubules and ßIVs-spectrin SD distribution			
ßIVs SD (veh)	186.8 ± 0.4	7.7 ± 0.4	0.61 ± 0.02
ßIVs SD (noco)	187.4 ± 0.1	8.5 ± 0.1	0.65 ± 0.02
Figure 7. The AIS nano-architecture is partially altered by inhibition of CK2 or elevated intracellular calcium			
ßIVs SD (ctrl)	187.9 ± 0.2	6.7 ± 0.2	0.58 ± 0.01
ßIVs SD (DMAT)	186.9 ± 0.1	7.0 ± 0.2	0.51 ± 0.01
ßIVs SD (KCl)	189.0 ± 0.3	17.8 ± 2.9	0.27 ± 0.01

Table S1. Spacing and periodicity measurements
The distribution of spacing values obtained by fitting sinusoids on intensity profiles is fitted by a Gaussian curve. The mean of this Gaussian is the "Mean spacing" column, and the standard deviation of this Gaussian is the "Spread" column. Errors are obtained from the fit procedure. The "R squared" column shows values for the goodness of sinusoid fit for all profiles in a given condition. All values are mean ± SEM. * same dataset (actin treated with vehicle) used in both figures.

bioRxiv preprint doi: https://doi.org/10.1101/022962; this version posted July 21, 2015. The copyright holder for this preprint (which was not certified by peer review) is the author/funder. All rights reserved. No reuse allowed without permission.

Labeling	Distance (nm)
Figure 4. The ankG CTer domain penetrates in the axoplasm, resulting in a radial orientation of ankG	
Nav	7.8 ± 1.3
a-tubulin	-84.8 ± 3.8
ankG SB	6.2 ± 1.2
ankG CTer	-26.1 ± 1.0
Figure 5. The 270- and 480-kDa isoforms of ankG have a similar radial extent	
ankG tail480	-1.8 ± 1.6 (distance to ankG CTer)
Figure 6. Radial orientation of ankG is resistant to actin or microtubule perturbation	
ankG CTer (veh)	-24.0 ± 1.1
ankG CTer (latA)	-25.6 ± 1.5
ankG SB (veh)	5.4 ± 1.6
ankG SB (noco)	5.0 ± 1.1
ankG CTer (veh)	-23.7 ± 1.4
ankG CTer (noco)	-25.3 ± 1.4
Figure 7. The AIS nano-architecture is partially altered by inhibition of CK2 or elevated intracellular calcium	
ankG CTer (ctrl)	-22.9 ± 1.4
ankG CTer (DMAT)	-27.5 ± 1.4
ankG CTer (KCl)	-22.3 ± 2.0

Table S2. Radial distance measurements
These distances are mean ± SEM obtained from measurements and fit on radial intensity profiles. Distance is to ßIV-spectrin SD labeling, unless specified otherwise.